Orco regulates the circadian activity of pheromone-sensitive olfactory receptor neurons in hawkmoths

Abbreviated title: Circadian regulation by Orco

Author names and affiliations:
* Aditi Vijayan, Animal Physiology and Center for Interdisciplinary Nanostructure Science and Technology, FB 10, University of Kassel, 34132 Kassel, Germany
* Mauro Forlino, Theoretical Physics and Center for Interdisciplinary Nanostructure Science and Technology, FB10, University of Kassel, 34132 Kassel, Germany
Yajun Chang, Animal Physiology and Center for Interdisciplinary Nanostructure Science and Technology, FB 10, University of Kassel, 34132 Kassel, Germany
Pablo Rojas, Theoretical Physics and Center for Interdisciplinary Nanostructure Science and Technology, FB10, University of Kassel, 34132 Kassel, Germany
Katrin Schröder, Animal Physiology and Center for Interdisciplinary Nanostructure Science and Technology, FB 10, University of Kassel, 34132 Kassel, Germany
Anna C. Schneider, Animal Physiology and Center for Interdisciplinary Nanostructure Science and Technology, FB 10, University of Kassel, 34132 Kassel, Germany
Martin E. Garcia, Theoretical Physics and Center for Interdisciplinary Nanostructure Science and Technology, FB10, University of Kassel, 34132 Kassel, Germany
Monika Stengl, Animal Physiology and Center for Interdisciplinary Nanostructure Science and Technology, FB 10, University of Kassel, 34132 Kassel, Germany
*Both authors contributed equally
Corresponding author email address: anna.c.schneider@uni-kassel.de

Conflict of interest: Authors report no conflict of interests.

Acknowledgements: We thank Dr. Dieter Wicher (Max Planck Institute for Chemical Ecology, Jena, Germany) for generously providing OLC15, and Rishaban Radhakrishnan for help with Python codes. We thank Prof. Hülya Altuntaş for helpful discussions.

Funding: AV, MF, YC, ACS, MEG, and MS were supported by Deutsche Forschungsgemeinschaft RTG 2749/1: “Biological Clocks on Multiple Time Scales”; KS and MS were supported by Deutsche Forschungsgemeinschaft STE531/20-2.

Author contributions:

Conceptualization: AV, MF, MEG, MS; data curation: AV, MF, YC, PR, KS, ACS, MEG, MS; formal analysis: AV, MF, YC, PD, ACS; funding acquisition: MEG, MS; investigation: AV, MF, YC, KS; methodology: MF, PR, MEG, MS; project administration: ACS, MEG, MS; resources: MEG, MS; software: AV, MF, PR, MEG; supervision: MEG, MS; validation: AV, MF, YC, PR, KS, ACS, MEG, MS; visualization: AV, MF, YC, ACS, MS; writing – original draft: AV, MF, ACS, MEG, MS; writing – reviewing & editing: AV, MF, YC, ACS, MEG, MS.

1 Abstract

The mating behavior of nocturnal *Manduca sexta* hawkmoths is under strict temporal control. It is orchestrated via circadian- and ultradian oscillations in sex-pheromone stimuli as social zeitgeber. The extremely sensitive pheromone-detecting olfactory receptor neurons (ORNs) that innervate the long trichoid sensilla on the male's antennae are peripheral circadian clocks. They express the transcriptional-translational feedback loop (TTFL) circadian clockwork, best characterized in *Drosophila melanogaster*. In hawkmoths, it is still unknown whether or how the ORN's TTFL clockwork regulates the daily rhythms in pheromone-sensitivity and in temporal resolution of ultradian pheromone pulses as prerequisites to the temporal regulation of hawkmoth mating behavior.

We hypothesize that, rather than the slow TTFL clock, a more rapidly adaptive post-translational feedback loop (PTFL) clockwork, associated with the ORN's plasma membrane, allows for temporal control of pheromone detection via generation of multiscale endogenous membrane potential oscillations. The potential oscillations of the PTFL clock could rapidly synchronize to oscillations of pheromone stimuli at different timescales, thus enable the prediction of stimulus patterns as a mechanism for active sensing. With *in vivo* long-term tip recordings of long trichoid sensilla of male hawkmoths, we analyzed the spontaneous spiking activity indicative of the ORNs' endogenous membrane potential oscillations. Consistent with our hypothesis of a multiscale PTFL clock in hawkmoth ORNs, spontaneous spiking was modulated on ultradian and circadian timescales, with maximum activity at night. When we blocked the evolutionarily conserved olfactory receptor coreceptor (Orco), the circadian modulation was abolished but the ultradian frequency modulation of the spontaneous activity remained. Consistent with PTFL control, Orco was not under the circadian control of the TTFL clock. We could replicate the experimental data in a conductance-based computational model of Orco. In this model, Orco conductivity changed as a function of fluctuating 2nd messenger levels. This study demonstrates that a PTFL is sufficient to impose a circadian pattern on ORN sensitivity.

2 Significance statement

It is generally assumed that all circadian rhythms in an organism are driven by a transcriptional-translational feedback loop (TTFL) clock. In this study, we demonstrate with *in vivo* recordings of hawkmoth pheromone-sensitive olfactory receptor neurons (ORNs) that the olfactory

receptor coreceptor (Orco) is the key pacemaker channel for controlling circadian but not ultradian rhythms in spontaneous spiking activity. Since Orco expression is not driven by the TTFL clock, its conductance is rather controlled by a post-translational feedback loop (PTFL) membrane clock. Accordingly, our computational model suggests that periodic changes in the conductivity of an Orco ion channel, which is mediated by cycling levels of cyclic nucleotides, tune ORN sensitivity. This highlights the role of the contribution of posttranslational modifications to the generation of circadian rhythmicity.

3 Introduction

Biological clocks generate endogenous physiological and behavioral oscillations on multiple timescales that persist in the absence of any external timing cues under constant conditions (Lamont and Amir, 2010). Such clocks are essential to generate internal rhythms and to permit their synchronization to external zeitgebers at timescales from milliseconds to years. These synchronized endogenous multiscale clocks thus provide both a continuous time frame for physiology and behavior - the organism's "present time" - and enable organisms to predict and respond to both regular, periodic environmental changes (Stengl and Schneider, 2024). Even though endogenous clocks are widespread in prokaryotes and eukaryotes (Géron et al., 2024; Hall and Rosbash, 1993; Millar, 2016; Thaiss et al., 2014), current knowledge about how multiscale clocks are linked over widely diverging timescales remains sparse.

Insect circadian clock neurons, which are tightly connected to visual brain circuits, are amongst the best studied biological clocks (Hall and Rosbash, 1993; Nishiitsutsuji-Uwo and Pittendrigh, 1968; Reinhard et al., 2024). They regulate physiological and behavioral oscillations that underly sleep-wake rhythms tied to the 24 h light-dark cycles on Earth (Dubowy and Sehgal, 2017). Circadian clock neurons possess a molecular clockwork of transcriptional-translational feedback loops (TTFLs), which generate endogenous oscillations of clock gene mRNA and protein levels with a cycle period of ~24 h (Hardin, 2011). It is assumed for both insects and mammals that this TTFL comprises the master clockwork that regulates all physiological and behavioral rhythms in the circadian time range through genetically controlled output pathways (Hastings et al., 2020).

Molecular TTFL clockworks were not only found in central brain clock neurons but also in sensory neurons, such as olfactory receptor neurons (ORNs) in insect antennae, where they play a role in odor-dependent circadian behaviors like feeding, pollination, reproduction, and navigation

100 (Flecke et al., 2010; Flecke and Stengl, 2009; Krishnan et al., 1999; Merlin et al., 2009, 2006; Page
101 and Koelling, 2003; Plautz et al., 1997; Sauman and Reppert, 1998; Schendzielorz et al., 2015;
102 Schuckel et al., 2007; Tanoue et al., 2004; Zhou et al., 2005). Little is known about how the TTFL
103 clockwork of insect ORNs regulates circadian rhythms in chemosensory sensitivity that underlie
104 the circadian control of these different behaviors.

105 At night, male nocturnal *Manduca sexta* hawkmoths are very sensitive to the sex pheromone
106 blend that their conspecific females release in an intermittent pattern (Itagaki and Conner, 1988).
107 The intermittency is a prerequisite to maintain the male's search flight, which is suspended at
108 pulse frequencies >30 Hz (Baker et al., 1985; Baker and Vogt, 1988; Stengl, 2010). The pheromone
109 pulses are resolved of up to 3 Hz by pheromone-specific ORNs in the antenna's long trichoid
110 sensilla (Lee and Strausfeld, 1990; Marion-Poll and Tobin, 1992). Pheromone-specificity is provided
111 by odor receptor (OR) subunits in the ciliary membranes of ORNs that heteromerize with the
112 conserved olfactory receptor co-receptor Orco (Nakagawa and Vosshall, 2009; Stengl and Funk,
113 2013; Wicher and Miazzi, 2021). While the various roles of Orco are still under debate, it is known
114 that in heterologous expression systems Orco homomers form a slow, leaky, non-specific cation
115 channel, which depolarizes the cells (Jones et al., 2011; Sargsyan et al., 2011; Sato et al., 2008;
116 Wicher et al., 2008). *In vivo* tip recordings of long trichoid sensilla in *M. sexta* confirmed that Orco
117 acts as spontaneously opening cation channel, acting as a pacemaker channel, because it
118 promotes ultradian membrane potential oscillations that underly the spontaneous action potential
119 activity (Nolte et al., 2013). These potential oscillations turn the ORNs into ultradian temporal
120 filters that are sensitive to the frequency of the pheromone pulses they encounter. Pheromone
121 pulses that arrive at a similar frequency as the endogenous sub-threshold membrane potential
122 oscillations would synchronize these oscillations and would be more likely to elicit action potential
123 trains. Therefore, this pacemaker channel-dependent mechanism would allow for active sensing if
124 endogenous membrane potential oscillations are in the physiological range necessary for tracking
125 intermittent pheromone pulses.

126 It is not known whether the Orco-dependent membrane potential oscillations also occur at
127 circadian timescales, and whether or how they are linked to ultradian potential oscillations. One
128 hypothesis is that the molecular TTFL clockwork of ORNs exclusively controls endogenous
129 circadian rhythms of the membrane potential via circadian expression of the pacemaker channel
130 Orco. Alternatively, the plasma membrane of ORNs could by itself constitute an autonomous clock
131 that is entrained by but does not rely on the TTFL clock. Constant levels of ion channels that do not

132 require daily degradation and daily transcription via the TTFL clock, but with modulation of open-
133 time probability by posttranslational modifications, would constitute a more economical and
134 faster adjustable mechanism to generate endogenous membrane potential oscillations (Stengl and
135 Schneider, 2024). This would facilitate active sensing, the rapid tuning to detect behaviorally
136 relevant zeitgeber signals in the insect's environment.

137 Here, we performed a combination of experimental and computational modeling studies to
138 investigate whether Orco plays a role in active sensing at the circadian and/or ultradian timescale
139 via generation of endogenous membrane potential oscillations. We hypothesize that Orco is part of
140 a post-transcriptional feedback loop (PTFL) clockwork in the plasma membrane, rather than being
141 TTFL controlled. To capture naturally occurring, physiologically relevant processes in insect ORNs
142 we performed *in vivo* long-term tip recordings of the spontaneous spiking activity of pheromone-
143 sensitive trichoid sensilla of intact but restrained hawkmoth males.

144 We corroborated the experimental data with a Hodgkin-Huxley (HH) based computational
145 ORN model. In general, the widely used deterministic HH models do not include circadian control
146 of ion channels. Moreover, the highly dynamic, bursting firing patterns of ORNs cannot be
147 described by the traditional deterministic modeling of neuronal activity. This constitutes a
148 drawback because stochasticity plays a crucial role in shaping firing patterns which are influenced
149 not only by external stimuli but also by the inherent noise involved in channel gating. Therefore, to
150 address the above points realistically, we developed a Langevin formulation of the HH model,
151 which explicitly accounts for the noise introduced by the random opening and closing of ion
152 channels and circadian modulation of the Orco channel conductivity. By integrating channel noise,
153 we could explore how circadian regulation of ionic currents contributes to the variability of firing
154 patterns and how this noise interacts with external stimuli to influence olfactory signal processing.

155 Our model aims to highlight the advantages of using a stochastic framework for modeling the
156 circadian activity of ORNs. The combined experimental and modeling efforts generate a more
157 complete picture and predictions concerning these autonomous processes in sensory neurons,
158 which are required for future exploration of physiologically relevant anticipatory behaviors that are
159 driven by biological clocks.

4 Methods

4.1 Animals

Nocturnal *M. sexta* hawkmoths were bred and raised from eggs in the rearing facility at the University of Kassel. Males and females were separated during pupal stages. Males were housed isolated from the females to avoid exposure to female pheromones. All experiments were performed with adult males reared in a long-day photoperiod (L:D 17:7 h to prevent diapause) at 25 °C with relative humidity of about 55%. Larvae were fed with an artificial diet modified after Bell and Joachim (1976); adult moths could feed on sugar solution with added vitamins (Roth) *ad libitum* (Riffell et al., 2008).

4.2 Solutions

Ringer compositions were taken from (Pézier et al., 2007) and contained (in mM): 6.4 KCl, 12 $MgCl_2$, 1 $CaCl_2$, 12 NaCl, 10 HEPES, 340 glucose for hemolymph ringer (HLR) at 450 mosmol/kg, and 172 KCl, 3 $MgCl_2$, 1 $CaCl_2$, 25 NaCl, 10 HEPES, 22.5 glucose for sensillum lymph ringer (SLR) at 475 mosmol/kg, both at pH 6.5. The Orco antagonist OLC15 (N-(4-butylphenyl)-2-((4-ethyl-5-(2-pyridinyl)-4H-1,2,4-triazol-3-yl)thio)acetamide (Chen and Luetje, 2012); kindly provided by Dr. D. Wicher, Max Planck Institute for Chemical Ecology, Jena, Germany) was dissolved in DMSO to a concentration of 100 mM (stock solution stored at 4-8 °C) before being diluted in SLR to a final concentration of 50 µM immediately before the start of the recording. DMSO percentage in the final solution was 0.05%.

4.3 Electrophysiology

The spontaneous electrical activity of the unstimulated pheromone-sensitive ORNs in a single long trichoid sensillum was recorded extracellularly as *in vivo* tip recording (Kaissling et al., 1987). 1-2-d-old male *M. sexta* that were raised in isolation from females and pheromone exposure were fixed in a custom-made Teflon holder with adhesive tape. The right antenna used for recordings was oriented with its dorsal surface facing up and immobilized near the base with dental wax (Boxing wax strips, KerrHawe SA). Electrodes (Ag/AgCl wire in a glass pipette filled with SLR for the recording electrode and HLR for the reference electrode) were pulled (DMZ-Universal Puller, Zeitz Instruments) from borosilicate capillaries (OD:1.56mm, ID: 1.17mm, without filament; Science Products) to a tip diameter of about 2 µm. After cutting off 20 distal annuli of the antenna

189 with micro scissors, the reference electrode was inserted into the antennal lumen up to the second
190 annulus from the cut end. The cut was covered with electrode gel (GE Medical Systems Information
191 Technology) to prevent desiccation. Electrodes were moved with manual micromanipulators (MMJ,
192 Märzhäuser Wetzlar; and Leitz, Leica Microsystems) or with motorized micromanipulators
193 (Microstar, Scientifica) with a joystick controller (Scientifica). Under microscopic control, some
194 tips of the long trichoid sensilla of the distal second annulus were cut off with sharpened Dumont
195 forceps, and the recording electrode slipped over a single sensillum of an upper sensillar row.
196 ORN activity was amplified 200-fold (custom built amplifier with 10^{12} Ω input impedance, or
197 ELC-01 MX in combination with DPA-2FX, npi, or EXT 10-2F, npi), low pass filtered at 1.3 kHz,
198 digitized at 20 kHz with a Digidata (1550A or 1550B, Molecular Devices), and saved for offline
199 analysis with Clampex 10 (pCLAMP suite, Molecular Devices).
200 All tip recording experiments were performed at room temperature (21-27 °C) and a relative
201 humidity of 35-60%. We recorded ORN activity either in long-day conditions (17:7 LD) or constant
202 darkness (DD) to examine the free-running peripheral ORN clock. For LD experiments, the light
203 regime continued as in the rearing facility during the experiment. For DD and OLC15 experiments,
204 the lights were turned off at the beginning of the recording, i.e. all animals were exposed to the
205 same zeitgeber until the beginning of the experiment. To examine the effect of Orco on the
206 spontaneous action potential (AP) activity pattern, we used the recording electrode to infuse
207 OLC15 in DD conditions.

208 **4.4 Data analysis**

209 To characterize the spontaneous ORN spiking activity, we first detected spikes with a self-
210 written program in Python. Using the scipy.signal package and find_peaks function, we applied a
211 Bessel filter to the raw voltage trace to facilitate spike detection within the following conditions:
212 spike full width (3-15 ms), threshold search for amplitude of spike (0.5-2.5 mV) and threshold
213 prominence (0.1). Two or more consecutive spikes with intervals ≤ 50 ms were considered a burst
214 (Dolzer et al., 2001). We then calculated the following attributes in bins of either 10 min or 1 h for
215 further analysis: instantaneous spike frequency (1 / inter-spike interval (ISI)), inter-burst interval
216 (IBI, time between two consecutive bursts with no single spikes in between), inter-event interval
217 (IEI, time between two events, i.e. two consecutive single spikes, two consecutive bursts, a burst
218 and a consecutive spike, and vice versa), burst duration (time from first to last spike in a burst),

219 percentage of all spikes in the experiment that are members of burst, and mean number of spikes
220 per burst (Figure 1). All statistics were done with those binned values.
221 Hawkmoth behavioral and physiological rhythms desynchronize across the population in the
222 absence of zeitgebers like pheromone stimulation and light-dark cycles. Therefore, it was
223 necessary to phase align the recordings obtained in DD and OLC15. To achieve this, we used an
224 optimization procedure to calculate the optimal temporal lags for each dataset, aiming to
225 maximize the overall cross-correlation between the calculated binned spike frequency series. The
226 optimization was performed using simulated annealing, which provided a set of time shifts (lags)
227 for each series. These lags were applied to shift the frequency data in a manner that maximized the
228 synchronization between the different subjects' data, resulting in a "subjective ZT" with subjective
229 ZT 0 at the first maximum of the binned ISI for each individual. The objective function used for
230 optimization was the negative sum of pairwise correlations between all series after applying the
231 shifts. The resulting alignment allowed us to compare the frequency patterns across the different
232 conditions.
233 Once the data were aligned, we computed the mean frequency across all subjects for each
234 bin and each condition. Then, the first high activity period was identified by finding the maximum in
235 the mean frequency series. Subsequently, we identified the second high activity period as the time
236 24 hours after the first one and the first low activity period was found by locating the minimum in
237 the mean frequency series between the two high activity periods.
238 Besides the mean frequency, we also searched for significant oscillations in IBI, IEI, burst
239 duration, percentage of spikes that are part of burst, and mean number of spikes per burst. For this
240 we found the maximum value of these statistics within a 3 h range centered in the first low activity
241 period and compared it with the values at the second high activity period.
242 Continuous wavelet and Fourier analysis were performed using PyBoat (Mönke et al., 2020)
243 to examine the time series of neuronal firing frequency. The continuous wavelet method allows us
244 to detect and characterize rhythmic patterns within the data by identifying frequency components
245 that change over time. Specifically, we used wavelet analysis to determine whether the neuron
246 exhibits circadian and ultradian rhythms. Unlike traditional Fourier analysis, which provides an
247 overall frequency composition but assumes stationarity, wavelet analysis is particularly useful for
248 biological signals because it can reveal how these frequencies evolve dynamically. By applying this
249 approach, we could assess not only the presence of ultradian rhythms but also whether their

strength or occurrence fluctuated in a circadian manner, indicating modulation by the 24-hour cycle.

4.5 Real-time quantitative polymerase chain reaction (qPCR)

We followed the qPCR methodology detailed in (Schneider et al., 2025). Briefly, male moths were isolated and cultured until the second day after eclosion, and the antennae from four individuals were collected at each zeitgeber time (ZT) 1, ZT9, and ZT17 using liquid nitrogen, with three biological replicates per time point. Total RNA was extracted using TRIzol® Reagent (Invitrogen) and quantified for concentration and purity with the NanoDrop ND-1000 spectrophotometer (Thermo Fisher Scientific). First-strand complementary DNA (cDNA) was synthesized using the PrimeScript™ RT reagent Kit with gDNA Erase (Takara Bio Inc.). Primers (F: AAGCACGTGGTCAGATTGGT, R: GTAAGCCAGGAGCGTCAGAG) for *Orco* (Gene ID: LOC115452348) were designed using the Primer-BLAST online program of NCBI. The qPCR was conducted following the protocol of TB Green® Premix Ex Taq™ II (Tli RNase H Plus) (Takara Bio Inc.), with the program: 95 °C for 30 s, followed by 40 cycles of 95 °C for 5 s, and 60 °C for 30 s. Relative expression levels of *Orco* were calculated using the $2^{-\Delta\Delta Ct}$ method (Livak and Schmittgen, 2001).

4.6 Statistics

All statistics were done with self-written python codes, SigmaPlot 12 (Systat Software), or JASP (version 0.19.03, University of Amsterdam) with a significance level $\alpha = 0.05$. Unless noted otherwise, data were checked for normal distribution with Anderson-Darling or Shapiro-Wilk tests and for equal variance with Levene's test. If one of these assumptions failed, we used non-parametric tests, otherwise we used parametric tests.

To assess the statistical significance of observed differences in neuronal activity of the aligned data between ZTs, we applied the Wilcoxon signed-rank test to pairwise comparisons between the first low activity period and the subsequent high activity period and discarded the transient high activity at the beginning of most recordings.

For other data, we used an ANOVA on ranks with either Tukey's or Dunn's post-hoc test for multiple comparisons as indicated.

4.7 ORN Model

In this study, we introduce a single-compartment Hodgkin-Huxley (HH) type model of the spontaneous activity of *M. sexta* ORNs. The model contains 5 sets of ion channels that were

280 previously identified in electrophysiological recordings (Dolzer et al., 2021): the fast sodium (Na^+)
281 and potassium (K^+) channels responsible for the generation of spikes, low voltage-activated
282 calcium channels (LVA) responsible for the initiation of bursts, calcium-gated potassium channels
283 (BK) responsible for the termination of bursts, and the Orco channel, which is a voltage-
284 independent non-specific, cAMP-gated channel. A schematic of the model is provided in Figure 2A.
285 We modeled Orco as a ZT-dependent conductance to represent the effect of the oscillations in
286 cAMP concentration that were identified in these cells (Schendzielorz et al., 2014) (Figure 2B, C).
287 For simplicity we chose to use a sine function to directly represent the oscillations in Orco
288 conductivity, but similar results can be achieved by modeling it as an output of a Goodwin model of
289 the circadian clock via cAMP concentration.

290 Each type of ion channel possesses one or more gates that can open and close individually
291 with transition rates α and β for opening and closing, respectively, of activation gates (n, m) and
292 inactivation gates (h). As a result, each possible combination of open and closed gates defines a
293 possible state in which each ion channel can be found. A schematic of the Markov chain depicting
294 all possible states and transitions for each ion channel is shown in Figure 2D. Each ion channel can
295 conduct current only in the state where all its gates are open.

296 First, we constructed a deterministic 22-dimensional model to serve as the mean field of the
297 Langevin model following the methodology proposed by Pu and Thomas (2020). Here, one
298 dimension tracks the membrane potential, another the intracellular Ca^{2+} concentration, and the
299 remaining 20 dimensions track the number of channels that are in a specific state of the Markov
300 chains. Considering the conservation of the total number of ion channels, each type of ion channel
301 required one less dimension than the total possible states.

302 The complete Langevin model adds to the mean field an independent noise source for each
303 transition in the Markov chain. These noise sources are biophysically motivated since the transition
304 between ion channel states is a stochastic process, with the probability of transition determined by
305 the kinetics of each kind of ion channel. The variability in the spiking behavior of a neuron emerges
306 from this non-deterministic gating of individual ion channels. The detailed mathematical
307 description of the model can be found in the Supplementary Material.

5 Results

We tested the hypothesis that sensory neurons, such as insect ORNs, perform active, anticipatory sensing based upon an endogenous, plastic plasma membrane clock with the pacemaker channel Orco as the core element. We focused on pheromone-sensitive long trichoid sensilla of male *M. sexta* hawkmoth antennae which exhibit daily rhythms in pheromone sensitivity and temporal resolution that are controlled by a circadian clock. We performed minimally invasive *in vivo* tip-recordings over the course of several days to search for daily rhythms in spontaneous spiking activity as a measure of endogenous membrane potential oscillations.

5.1 Pheromone-sensitive hawkmoth ORNs exhibit Orco-dependent circadian rhythms in spontaneous spiking activity

The ORNs that innervate the pheromone-sensitive long trichoid sensilla on male *M. sexta* antennae display spontaneous spiking patterns of irregular bursts with interspersed single action potentials in short-term recordings (Dolzer et al., 2001). In the present study we documented the same pattern in long-term recordings over the course of several days. This enabled us to search for daily and circadian rhythmicity in spontaneous ORN spiking activity in the absence of pheromone stimulation.

The spontaneous spiking patterns revealed clear daily rhythms in 5 of 11 animals under long-day conditions (17:7 h LD) (Figure 3A). The maxima in spontaneous activity occurred mostly during the dark phase when nocturnal hawkmoths are active (Figure 3A (top), Bi light blue arrow), and minima occurred during the light phase when hawkmoths rest/sleep (Figure 3A (bottom), Bi dark blue arrow). High spiking activity in the dark phase had a mean maximum frequency of ~3 Hz (theta range: 0.5 – 4 Hz) (Figure 3Bii). In contrast, the minimum spiking frequencies during the hawkmoth's resting phase were below 0.5 Hz (Figure 3A (bottom)). Since ORN firing patterns had a clear daily rhythm in LD both in individual animals (Figure 3Bi) and averaged across animals (Figure 3Bii, Biii), we examined whether these rhythms depended on cycling light cues or whether they persisted in constant darkness (DD), as expected for an endogenous, circadian clock-driven rhythm.

In DD, the spontaneous ORN firing pattern remained rhythmic (7 of 10 animals), albeit with less robustness: The single peak of high spiking activity that was observed at the same ZT across several days in LD divided into multiple bouts of high spiking activity in the activity phase in 7 of 10 animals (Figure 3Ci). Also, in DD conditions, the high spiking activity phase shifted into the

subjective day due to the individual endogenous circadian periods of about 23.5 h +/- 2.8h (21.27 h in Figure 3Ci). Thus, averaging the instantaneous spiking activity across all DD animals did not depict clear circadian rhythms (Figure 3Cii). Therefore, we phase-aligned the mean frequency of spontaneous activity (see Methods). After alignment, circadian rhythms were exposed across DD animals (Figure 3Ciii), comparable to the daily rhythms in LD (cf. Figure 3 Biii and Ciii).

Next, we examined whether Orco, a leaky, non-specific cation channel, is the dominant depolarizing pacemaker current of ORNs that drives circadian rhythms in spontaneous spiking activity. Infusion of the Orco antagonist OLC15 into the sensillum lymph obliterated circadian rhythms and attenuated the spontaneous activity in several, but not all experiments (N = 8 of 12) (Figure 3Di). This attenuation resulted in a linear decrease in spiking activity over several days (Figure 3Dii, Diii). Even after phase-aligning the individual experiments, no circadian rhythm was present in the average across all OLC15-treated animals (Figure 3Diii).

Because OLC15 is not membrane-permeable on its own it was infused with low concentrations (0.05%) of DMSO through the recording electrode into the sensillum lymph and, therefore, effectiveness increased over time. Hence, we fit the spiking activity of each animal and in each condition with linear regression lines over the whole recording time to compare the slopes of the fits (Figure 3E). In LD, the mean ± SD slope was 0.004 ± 0.006 Hz/h, indicating that the average spiking activity remained similar throughout the duration of the recording. In DD, the slope was -0.003 ± 0.018 Hz/h and was not different from LD. In contrast, the mean slope during OLC15 treatment was -0.007 ± 0.022 Hz/h, significantly smaller than in LD (ANOVA on ranks with Dunn's post-hoc test; $H(2) = 7.681$, $p = 0.021$). The negative slope corroborated the finding that spiking activity decreased over time in the presence of the Orco blocker.

Activity rhythms between hawkmoths desynchronize and have only weak phase coupling in the absence of pheromone stimulation, even in LD cycles (Ghosh et al., 2024). Therefore, instead of comparing fixed ZT or circadian time (CT) intervals, we compared different attributes of spontaneous activity between periods of high and low activity, for DD conditions after phase alignment (see Methods; Figure 4). Despite the high variability in ORN spiking between individuals, the mean frequency of spontaneous ORN activity was significantly higher during the high activity phase than during low activity in both LD and DD recordings (Figure 4Ai, Aii). In LD but not in DD, the frequency of bursting increased significantly during the high activity phase (Figure 4Bi, Bii). The percentage of spikes that are part of bursts was less variable and lower during the high activity phase in LD but not significantly different in DD (Figure 4Ci, Cii). The mean burst duration was less

variable during the high than the low activity phase in LD, but not significantly shorter in any condition (Figure 4Di, Dii). Furthermore, both in LD and DD, the mean inter-event frequencies were significantly higher during the high activity phase (Figure 4Ei,Eii), indicating a significantly higher overall spontaneous spiking activity during the hawkmoth's activity phase. The mean number of spikes per burst, and intra-burst frequencies did not differ significantly between high or low activity periods in both LD and DD conditions (Figure 4Fi, Fii, Gi, Gii). The addition of Orco antagonist OLC15 deleted any significant differences of spontaneous activity found in LD and DD (Figure 4Aiii-Giii). In conclusion, the mean frequency of spontaneous spiking and the frequency of bursting expressed daily modulation, and are both most likely controlled via a circadian clock that targets the leak channel Orco.

5.2 Orco imposes circadian modulation on the ultradian rhythms in spontaneous ORN activity

After establishing that Orco influences the circadian changes in ORN spiking activity between the animal's resting and activity phase we examined if Orco also influences ORN spiking rhythms on the largely different ultradian timescales in the frequency range between 0.01-1000 Hz. In all conditions, two broad bands of ultradian instantaneous frequencies were evident: one upper band of >10 to ~100 Hz and a lower band between 0.1 to ≤10 Hz (Figure 5). The upper band primarily represents the frequencies of spikes within a burst, while the lower band represents single spikes and frequencies between bursts.

In LD, two types of daily/circadian modulation of the ultradian frequencies occurred (Figure 5A). The upper higher frequency band was mostly modulated in prevalence (its frequency of occurrence) but not in its frequency range. The lower band was modulated both in prevalence and frequency range, which resulted in a sinusoidal change in the mean of the frequency band over 24 h. The low and high frequency bands appeared to merge during the activity phase around ZT 0 in the animals that showed clear circadian rhythms (N = 5 of 11 in LD), when both bands had maximum prevalence. During the hawkmoth's activity phase, higher frequencies of up to ~10 Hz occurred, while frequencies dropped below 1 Hz during the resting phase.

The circadian modulation of both frequency bands was maintained in constant darkness (Figure 5B) but phase-shifted with respect to the projected ZT due to the endogenous circadian period of each individual. Again, this indicates that a clock is modulating the spontaneous ORN spiking activity over the course of a day.

402 The addition of the Orco antagonist OLC15 deleted any circadian modulation of either
403 frequency band. Interestingly, the instantaneous frequencies in both bands still showed correlated
404 changes in prevalence and merging, but now at ultradian periods only.
405 Additional Fourier analysis (see Methods) of spontaneous spiking activity over the course of
406 several days revealed faster ultradian and slower infradian rhythms, ranging from 0.6 h to 38 h, in
407 addition to the circadian (24 ± 4 h) rhythm (Figure 6Ai, Bi, Ci). Some rhythms (factorials of 24 h, like
408 12 h, 6 h, etc.) appeared to be harmonics of the circadian rhythm, which were not excluded in our
409 analysis. Most animals expressed ultradian rhythms of 2-4 h in LD as well as DD conditions. With
410 OLC15 the occurrence of circadian rhythmicity decreased from 70% to 33.3 %, while the
411 prevalence of infradian periods increased from 0% to 33.3 % and ultradian periods remained the
412 same. These results were corroborated by continuous wavelet analysis, which provided time-
413 resolved spectral power across different rhythmic periods (Figure 6Aii, Bii, Cii).In control LD and DD
414 conditions, wavelet power for ultradian periods increased during times of elevated firing rate and
415 decreased during periods of low activity (Figure 6Aii and Bii, middle and bottom panels). This
416 dynamic pattern indicates that ultradian rhythms were not constant over time but were instead
417 modulated by the circadian rhythm, becoming more prominent during circadian peaks in neuronal
418 activity. Such circadian gating of ultradian power was clearly visible in the wavelet spectrograms as
419 alternating bands of higher and lower ultradian power aligned with daily activity cycles. Following
420 Orco blockade with OLC15, this modulation was disrupted (Figure 6Cii middle panel): although
421 ultradian components persisted (Figure 6Cii bottom panel), they no longer showed systematic
422 variation with the circadian cycle, suggesting a decoupling of ultradian rhythms from circadian
423 control.

424 5.3 Orco expression is not under the control of the molecular TTFL clockwork

425 So far, our results indicated a prominent role of Orco in the circadian modulation of ORN
426 spiking activity. Since it is the general opinion that the master circadian clock that dominates all
427 physiological and behavioral circadian rhythms functions via transcriptional control we examined
428 whether Orco transcription shows a circadian rhythm, as previously found for clock genes in
429 hawkmoth antennae (Schneider et al., 2025; Schuckel et al., 2007). However, qPCR of whole male
430 hawkmoth antennae revealed no significant circadian rhythm of Orco expression in DD (Figure 7;
431 ANOVA on ranks, $H(2) = 5.60$, $p = 0.061$). Thus, it is possible that Orco is controlled via a

posttranslational circadian clockwork mechanism that is associated directly with the plasma membrane (Stengl and Schneider, 2024; Stengl and Schröder, 2021).

5.4 Circadian changes in Orco conductance are sufficient to modulate spiking activity in a computational model of a hawkmoth ORN

Although Orco is a leaky ion channel, its maximum conductivity is modulated by cAMP (Getahun et al., 2013; Martín et al., 2001; Sargsyan et al., 2011; Wicher et al., 2008). In hawkmoth antennae, cAMP levels oscillate throughout the day (Dolzer et al., 2021; Flecke et al., 2010; Flecke and Stengl, 2009; Schendzielorz et al., 2014, 2015), which makes cAMP modulation of Orco a putative mechanism for the Orco-dependent circadian modulation of ORN spiking activity, integrating Orco in a circadian PTFL based membrane clockwork (Stengl and Schneider, 2024).

To test the hypothesis that Orco is a cAMP-gated, leaky ion channel, we constructed an ORN model (Methods and Supplementary Material) and tuned the parameters to provide a quantitative match with the biological data. The developed model provides a unified description of the experimental observations. For instance, the ORN model yields irregular spiking activity with a bimodal distribution, consisting of both bursts and isolated spikes, successfully reproducing the experimental recordings (Figure 8A). This suggests a unified mechanism underlying the initiation of both phenomena: If the pacemaker-driven depolarization reaches the Na^+ threshold a firing process begins, and at this point randomness determines if other slower ion channels responsible for bursting are sufficiently activated to sustain a burst of several spikes.

Additionally, the ORN model replicates the distribution of the number of spikes per burst, which follows a decreasing exponential trend in both experimental and simulated results (Figure 8B).The model also successfully reproduces the circadian modulation of spiking activity: the maximum firing rate occurs when the Orco conductance is maximal, whereas the maximum percentage of spikes that are part of bursts correlates with the lowest Orco conductance, resulting in antiphase oscillations, as were observed in the experimental recordings (Figure 9).

The frequency prevalences in the model over several days clustered in two distinct frequency bands: a top band that corresponds to the intra-burst frequencies and a bottom band, corresponding to inter-burst frequencies (Figure 10), in agreement with the biological experiments (Figure 5A, B). When these circadian oscillations in Orco conductance were included, inter-burst frequencies showed significant circadian variations, whereas intra-burst frequencies remained relatively constant, reminiscent of the biological data. Notably, the simulation captured the

experimentally observed "merging" effect, where the low frequency band approaches the top band during high-activity periods (Figure 10).

This merging of spiking and bursting frequencies suggests that the system approached a bifurcation, transitioning from a bursting regime to tonic spiking activity. Further evidence for the near bifurcation condition of the neurons is the distribution of number of spikes per burst that followed a decreasing exponential trend in contrast to a constant value, or a bounded range of spikes per burst, which would be expected from a standard bursting neuron model (Figure 8B). The observation that the circadian modulation of spiking activity requires only one parameter, namely changes in the Orco conductivity, to describe the circadian effects on the ORN spiking pattern indicates the crucial role of Orco channel in circadian control.

6 Discussion

We searched for a membrane-bound clockwork component in insect ORNs that allows for sensing of regular pheromone patterns to guide mating flights. For this, we recorded interlinked circadian and ultradian frequencies in the spontaneous spiking activity of the pheromone-sensitive long trichoid sensilla of male *Manduca sexta* hawkmoths with *in vivo* long-term tip recordings. We found that Orco, which serves several important functions in insect olfaction (Stengl and Funk, 2013; Wicher and Miazzi, 2021), acts as a pacemaker channel that controls the circadian modulation of the spiking activity without affecting the frequency ranges that are relevant for the primary fast, phasic pheromone response (Dolzer et al., 2003; Nolte et al., 2016; Schneider et al., 2025). While circadian rhythmicity disappeared in the presence of the Orco blocker OLC15, ultradian activity rhythms remained. We confirmed with computational modeling that the circadian modulation of open-time probability of Orco as a leaky pacemaker channel was sufficient to account for our experimental results. Since we observed no evidence for circadian transcriptional control of Orco, our findings are consistent with the hypothesis that the plasma membrane constitutes an endogenous post-translational feedback loop (PTFL) clockwork. In this clockwork, circadian changes in cyclic nucleotide levels (Schendzielorz et al., 2015) modulate Orco conductance rather than transcription and insertion of additional Orco channels in the membrane.

The expression of a pacemaker channel that does not require daily degradation and transcription would constitute an economic and rapidly adjustable mechanism to generate endogenous membrane potential oscillations that are tuned to detect behaviorally relevant

493 zeitgeber signals in the insect's environment (Stengl and Schneider, 2024; Stengl and Schröder,
494 2021). The present study provides the first evidence for a systems view of timing that involves a
495 PTFL membrane clock in hawkmoth ORNs, instead of the prevailing hierarchical view that assumes
496 all endogenous circadian oscillations are outputs of the genetic TTFL clock (Stengl and Schneider,
497 2024; Stengl and Schröder, 2021).

498 6.1 Orco acts as a pacemaker channel to drive the circadian rhythm in spontaneous 499 ORN spiking activity

500 A common motif of spontaneously active neurons is the expression of pacemaker channels
501 that open at hyperpolarized potentials and thus depolarize the neuron (Bose et al., 2014; Cochet-
502 Bissuel et al., 2014; Das et al., 2016; Golowasch et al., 2017; Lüthi and McCormick, 1998; Ratliff et
503 al., 2021; Robinson and Siegelbaum, 2003; Sharma et al., 2023). The resting membrane potential of
504 most neurons lies close to the negative equilibrium potential for potassium ions due to potassium
505 leak channels (Goldstein et al., 2001; Patel and Honoré, 2001; Talley et al., 2001). When the
506 pacemaker-driven depolarization reaches spike thresholds, voltage-gated Na^+, K^+ and Ca^{2+}
507 channels promote spiking. Voltage- and Ca^{2+}-gated K^+ channels then repolarize the neuron to
508 negative membrane potentials, re-starting the cycle

509 The core element of the different frequencies of endogenous oscillations that needs to be
510 identified is the respective pacemaker channel (Stengl and Schneider, 2024). The finding of distinct
511 rhythms in spontaneous spiking activity under constant conditions are indicative of underlying
512 endogenous membrane potential oscillations. Therefore, different sets of voltage- and Ca^{2+}-
513 dependent ion channels with antagonistic effects on the membrane potential appear to underlie
514 different ultradian oscillation frequencies of spontaneous activity that still need to be further
515 elucidated (Dolzer et al., 2021; Stengl, 1994, 1993; Zufall et al., 1991). While this study did not aim
516 to unravel the overall generation of spontaneous activity in the ORNs, we could demonstrate that
517 Orco acts as a circadian pacemaker channel that drives the circadian modulation of the spiking
518 activity.

519 6.2 The constitutively expressed Orco is a core element of a circadian PTFL 520 clockwork in hawkmoth ORNs

521 In hawkmoth ORNs, at least two types of pacemaker channels exist: the highly conserved,
522 slow, leaky Orco, which we focus on in this study, and an HCN type channel (Butterwick et al.,

523 2018; Dolzer et al., 2021; Nolte et al., 2016, 2013; Sato et al., 2008; Stengl and Funk, 2013; Stengl
524 and Schneider, 2024; Stengl and Schröder, 2021; Wicher et al., 2008; Wicher and Miazzi, 2021).
525 When expressed *in vitro* in heterologous expression systems, *Drosophila* Orco homomers
526 assemble into leaky, non-specific cation channels with a reversal potential around 0 mV,
527 constitutively leaking Na^+, K^+, and Ca^{2+} (Sato et al., 2008; Wicher et al., 2008; Wicher and Miazzi,
528 2021). In *Drosophila*, Orco is regulated by Ca^{2+}/calmodulin and phosphorylation/de-
529 phosphorylation at multiple sites (Cao et al., 2016; Getahun et al., 2016; Guo and Smith, 2017;
530 Mukunda et al., 2016, 2014; Sargsyan et al., 2011). In *Drosophila*, the Ca^{2+}/calmodulin binding site
531 controls the localization of the OR-Orco complex in the ciliary membrane of ORNs and depends on
532 previous odor stimulation (Cao et al., 2016; Guo and Smith, 2022; Jain et al., 2021). After
533 phosphorylation of Orco by protein kinase C (PKC), a cyclic nucleotide binding site becomes
534 available, and subsequent binding of cAMP or cGMP increases the open-time probability (Getahun
535 et al., 2013; Wicher et al., 2008). This indicates two complementary mechanisms by which Orco
536 conductance can be regulated: by controlling the number of Orco channels in the membrane or by
537 modulating the open-time probability of existing channels through posttranslational modifications.
538 Since blocking Orco in *M. sexta* decreased the spontaneous activity and deleted its circadian
539 modulation, Orco is apparently the main target for modulation of circadian activity in hawkmoth
540 ORNs. Since Orco transcription levels were constant, posttranslational modifications of Orco that
541 modulate the open-time probability provide a mechanistic explanation. Increases in cAMP and
542 cGMP levels sensitize or adapt the ORNs to pheromone, respectively (Dolzer et al., 2021, 2008;
543 Flecke et al., 2010, 2006; Redkozubov, 2000; Schendzielorz et al., 2015, 2012; Ziegelberger et al.,
544 1990). While cAMP levels are under circadian control and peak during the activity phase, cGMP
545 levels oscillate in a daily rhythm and peak during the resting phase in insects (Schendzielorz et al.,
546 2014, 2015). We propose that cAMP and cGMP binding modulate Orco with opposing effects,
547 consistent with the physiological needs of the hawkmoth during its sleep-wake cycle: cAMP
548 binding increases Orco conductance while cGMP binding decreases it.
549 Our hypothesis that a circadian PTFL membrane clock in hawkmoth ORNs controls circadian
550 activity rhythms predicts that the pacemaker channel Orco is part of a membrane signalosome.
551 The protein complexes of this signalosome would comprise the pacemaker channel that generates
552 the specific circadian frequency of endogenous potential oscillations, linked to oscillations of
553 second messenger cascades that determine physiological setpoints of the circadian sleep-wake
554 cycles. Thus, the circadian cAMP oscillations could result from a PTFL membrane clock comprising

555 of a signalosome that minimally consists of voltage-gated Ca^{2+}-channels, Orco, and membrane-
556 anchored adenylyl cyclases (ACs). Since the membrane potential directly influences intracellular
557 Ca^{2+} levels, the AC activity could be periodically upregulated by the circadian oscillations of the
558 endogenous membrane potential oscillations. Alternatively, AC expression could be under the
559 control of the molecular TTFL clock, which would put Orco under indirect TTFL control. This
560 possibility should be further explored in hawkmoth antennae. Instead of, or in addition to, the
561 voltage-gated Ca^{2+} channels the signalosome could also work if it contained octopamine receptors
562 that cause circadian rises in cAMP levels through activation of $G_{\alpha s}$, as found in hawkmoths (Dacks
563 et al., 2006; Flecke et al., 2010). Since octopamine levels in the hemolymph exhibit circadian
564 oscillations and octopamine sets a physiological state of heightened alertness in insects, the
565 circadian PTFL clock in ORNs would synchronize with endogenous physiological rhythms via
566 octopamine receptor activation (Flecke and Stengl, 2009; Schendzielorz et al., 2015).

567 **6.3 Circadian and ultradian rhythms in spontaneous ORN activity resemble the**
568 **physiologically relevant timescales for active sensing**

569 Moths are more sensitive to pheromone stimulation during their activity phase than at rest,
570 apparently due to antennal circadian clocks (Flecke et al., 2010; Flecke and Stengl, 2009; Merlin et
571 al., 2007, 2006; Schendzielorz et al., 2015; Schuckel et al., 2007; Silvegren et al., 2005). The greater
572 the distance from the female, the lower the pheromone concentration. The increased pheromone
573 sensitivity during the activity phase enhances the male's chance to detect a calling female.
574 Pheromone concentration is encoded in the frequency of the first, phasic burst of spikes of
575 the characteristic triphasic spiking sequence of ORNs in response to brief pheromone pulses,
576 which is independent of Orco (Dolzer et al., 2003; Nolte et al., 2013; Schneider et al., 2025).
577 However, through the cAMP-dependent increase in Orco conductance during the activity phase,
578 the ORN membrane potential is closer to spike threshold and fewer pheromone molecules are
579 necessary to produce a receptor current that brings the membrane voltage over that threshold.
580 Thus, larger Orco conductance increases the likelihood of an ORN response to pheromone
581 stimulation without changing the typical triphasic spiking pattern of the response.
582 In the odor transduction of *Drosophila*, OR-Orco activation drives the initial receptor current
583 response. In contrast, Orco is not part of an OR-Orco odor-gated receptor ion channel complex in
584 hawkmoths but controls the spontaneous ORN activity and the late, long-lasting pheromone
585 response (LLPR). The LLPR begins several hundred milliseconds after the initiation of the

586 pheromone-dependent transduction current and correlates with the time course of pheromone-
587 induced rises in cGMP levels (Boekhoff et al., 1993; Nolte et al., 2016, 2013; Stengl, 2010; Stengl et
588 al., 2001; Wicher and Miazzi, 2021; Ziegelberger et al., 1990). Thus, in hawkmoths, Orco is not part
589 of the primary transduction channel but rather controls membrane potential oscillations and
590 thereby the temporal resolution and general pheromone sensitivity of ORNs. The higher
591 spontaneous burst frequency during the hawkmoth's activity phase improves the resolution of the
592 anticipated pheromone pulses during its mating flight in search for females.
593 In the mammalian suprachiasmatic nucleus (SCN), the clock that controls the sleep-wake
594 cycle, cAMP levels oscillate at an ultradian frequency, and cAMP and cGMP induce opposing phase
595 shifts in SCN spiking activity (Prosser et al., 1989; Prosser and Gillette, 1991). In *M. sexta* antennae,
596 cAMP levels express daily oscillations and peak during the activity phase. In contrast, cGMP levels
597 do not oscillate but are elevated by pheromone exposure, which adapts the spiking activity
598 (Boekhoff et al., 1993; Dolzer et al., 2021; Flecke et al., 2006; Schendzielorz et al., 2015;
599 Ziegelberger et al., 1990). This implies that cAMP and cGMP may have opposing effects on Orco
600 conductivity, with results similar to what is seen in the SCN.
601 The upregulation of neural activity during wakefulness/alertness seems to be ubiquitous
602 among animals. For example, the many synchronously recorded neurons in human EEG show high
603 frequency oscillations in the beta and gamma ranges during alertness and low frequency
604 oscillations in the delta and theta ranges during rest and sleep. Similarly, the spontaneous spiking
605 activity of hawkmoth ORNs is upregulated during their activity phase, albeit only from below delta
606 to the delta/theta range. The increased spontaneous spiking activity in the theta range during the
607 activity phase of the hawkmoth matches the maximal temporal resolution of pheromone pulses of
608 up to 10 Hz (Marion-Poll and Tobin, 1992), which supports a role for Orco as part of a membrane-
609 bound PTFL clockwork that tunes the ORNs for active sensing. Even through oscillations in the field
610 potential of electroantennogram responses to odor stimulation can reach 100 Hz in different
611 insects (Szyszka et al., 2014), these frequencies most likely do not encode physiological odor
612 responses. Apparently, they reflect the astounding adaptive ability of antennal ORNs to
613 synchronize their endogenous membrane potential oscillations across the antenna to a broad
614 range of stimulation frequencies. Pheromone pulse resolution of about 100 Hz was never reported
615 in single olfactory sensilla recordings, and in behavioral experiments male moths stopped their
616 upwind mate search if pheromone pulses exceeded 30 Hz (Baker et al., 1985; Bau et al., 2005,
617 2002; Tripathy et al., 2010).

Circadian oscillations in the ORN membrane potential would be ideally suited to tune sensitivity and temporal resolution of the pheromone-sensitive ORNs to the hawkmoth's rest-activity cycle, synchronizing male and female mating behavior. Further experiments are needed to test our hypothesis that ORN signalosomes are highly plastic endogenous PTFL clocks comprising receptors for circadian and ultradian Zeitgebers that allow to tune into internal physiological and external environmental rhythms as basis for active sensing.

6.4 Stochastic ion channel dynamics and circadian modulation of Orco conductance explain modeled ORN firing patterns

Our modeling results provide mechanistic insight into the irregular spontaneous activity of pheromone-sensitive ORNs in *M. sexta*, highlighting how stochastic ion channel dynamics and circadian modulation of ion conductance together shape spiking patterns. By employing a Langevin approximation of the stochastic HH formalism, we demonstrate that the intrinsic noise arising from the random gating of ion channels is sufficient to generate both isolated spikes and bursts of spikes, as observed experimentally. Our model effectively recapitulates the spike distributions found *in vivo* and accounts for the role of channel noise as a critical determinant of ORN firing patterns.

A key contribution of our model is the incorporation of the Orco ion channel as a pacemaker component, with a conductance that varies linearly with cAMP concentration. We show that circadian modulation of Orco conductance alone is sufficient to produce the observed time-of-day dependent changes in spike distribution. This finding suggests that the rhythmic expression of cAMP levels across the circadian cycle may act as a primary driver of diurnal changes in ORN excitability, without requiring additional external inputs or modulation of other ion channels.

Importantly, our results reveal that the same set of ion channels can support the emergence of both single action potentials and complex bursting behaviors purely through the stochastic variability of their gating kinetics. This unifying explanation reduces the need for invoking separate biophysical mechanisms or circuit-level inputs to explain these distinct firing modes.

For simplicity, the circadian variation in cAMP concentration was modeled using a sinusoidal function. While this approximation is sufficient for capturing the qualitative features of the rhythmic modulation, future work could enhance the biological realism of the model by coupling Orco conductance dynamics to a molecular circadian oscillator, such as a Goodwin-type transcriptional-translational feedback loop. Incorporating this layer would allow for a more

649 detailed exploration of how molecular clock components regulate cAMP synthesis and
650 degradation. Additionally, further extensions could include downstream regulatory mechanisms
651 such as phosphorylation and dephosphorylation events mediated by kinases and phosphatases
652 under circadian control, potentially contributing to fine-tuned modulation of ion channel function
653 over the daily cycle.

654 Together, these findings demonstrate the value of a biophysically grounded, noise-inclusive
655 modeling framework for understanding complex temporal patterns in sensory neuron activity and
656 open the door for future integrative models linking molecular circadian clocks to cellular
657 excitability.

7 References

Baker TC, Vogt RG. 1988. Measured Behavioural Latency in Response to Sex-Pheromone Loss in the Large Silk Moth *Antheraea Polyphemus*. *J Exp Biol* **137**:29–38. doi:10.1242/jeb.137.1.29

Baker TC, Willis MA, Haynes KF, Phelan PL. 1985. A pulsed cloud of sex pheromone elicits upwind flight in male moths. *Physiol Entomol* **10**:257–265. doi:10.1111/j.1365-3032.1985.tb00045.x

Bau J, Justus KA, Cardé RT. 2002. Antennal resolution of pulsed pheromone plumes in three moth species. *J Insect Physiol* **48**:433–442. doi:10.1016/S0022-1910(02)00062-8

Bau J, Justus KA, Loudon C, Cardé RT. 2005. Electroantennographic Resolution of Pulsed Pheromone Plumes in Two Species of Moths with Bipectinate Antennae. *Chem Senses* **30**:771–780. doi:10.1093/chemse/bji069

Bell RA, Joachim FG. 1976. Techniques for Rearing Laboratory Colonies of Tobacco Hornworms and Pink Bollworms1. *Ann Entomol Soc Am* **69**:365–373. doi:10.1093/aesa/69.2.365

Boekhoff I, Seifert E, Göggerle S, Lindemann M, Krüger B-W, Breer H. 1993. Pheromone-induced second-messenger signaling in insect antennae. *Insect Biochem Mol Biol* **23**:757–762. doi:10.1016/0965-1748(93)90063-X

Bose A, Golowasch J, Guan Y, Nadim F. 2014. The role of linear and voltage-dependent ionic currents in the generation of slow wave oscillations. *J Comput Neurosci* **37**:229–242. doi:10.1007/s10827-014-0498-4

Butterwick JA, del Mármol J, Kim KH, Kahlson MA, Rogow JA, Walz T, Ruta V. 2018. Cryo-EM structure of the insect olfactory receptor Orco. *Nature* **560**:447–452. doi:10.1038/s41586-018-0420-8

Cao L-H, Jing B-Y, Yang D, Zeng X, Shen Y, Tu Y, Luo D-G. 2016. Distinct signaling of *Drosophila* chemoreceptors in olfactory sensory neurons. *Proc Natl Acad Sci* **113**:E902–E911. doi:10.1073/pnas.1518329113

Chen S, Luetje CW. 2012. Identification of New Agonists and Antagonists of the Insect Odorant Receptor Co-Receptor Subunit. *PLOS ONE* **7**:e36784. doi:10.1371/journal.pone.0036784

Cochet-Bissuel M, Lory P, Monteil A. 2014. The sodium leak channel, NALCN, in health and disease. *Front Cell Neurosci* **8**:132. doi:10.3389/fncel.2014.00132

Dacks AM, Dacks JB, Christensen TA, Nighorn AJ. 2006. The cloning of one putative octopamine receptor and two putative serotonin receptors from the tobacco hawkmoth, *Manduca sexta*. *Insect Biochem Mol Biol* **36**:741–747. doi:10.1016/j.ibmb.2006.07.002

Das A, Holmes TC, Sheeba V. 2016. dTRPA1 in Non-circadian Neurons Modulates Temperature-dependent Rhythmic Activity in *Drosophila melanogaster*. *J Biol Rhythms* **31**:272–288. doi:10.1177/0748730415627037

Dolzer J, Fischer K, Stengl M. 2003. Adaptation in pheromone-sensitive trichoid sensilla of the hawkmoth *Manduca sexta*. *J Exp Biol* **206**:1575–1588. doi:10.1242/jeb.00302

Dolzer J, Krannich S, Fischer K, Stengl M. 2001. Oscillations of the Transepithelial Potential of Moth Olfactory Sensilla Are Influenced by Octopamine and Serotonin. *J Exp Biol* **204**:2781–2794. doi:10.1242/jeb.204.16.2781

Dolzer J, Krannich S, Stengl M. 2008. Pharmacological Investigation of Protein Kinase C- and cGMP-Dependent Ion Channels in Cultured Olfactory Receptor Neurons of the Hawkmoth Manduca sexta. *Chem Senses* **33**:803–813. doi:10.1093/chemse/bjn043

Dolzer J, Schröder K, Stengl M. 2021. Cyclic nucleotide-dependent ionic currents in olfactory receptor neurons of the hawkmoth *Manduca sexta* suggest pull–push sensitivity modulation. *Eur J Neurosci* **54**:4804–4826. doi:10.1111/ejn.15346

Dubowy C, Sehgal A. 2017. Circadian Rhythms and Sleep in *Drosophila melanogaster*. *Genetics* **205**:1373–1397. doi:10.1534/genetics.115.185157

Flecke C, Dolzer J, Krannich S, Stengl M. 2006. Perfusion with cGMP analogue adapts the action potential response of pheromone-sensitive sensilla trichoidea of the hawkmoth *Manduca sexta* in a daytime-dependent manner. *J Exp Biol* **209**:3898–3912. doi:10.1242/jeb.02432

Flecke C, Nolte A, Stengl M. 2010. Perfusion with cAMP analogue affects pheromone-sensitive trichoid sensilla of the hawkmoth *Manduca sexta* in a time-dependent manner. *J Exp Biol* **213**:842–852. doi:10.1242/jeb.032839

Flecke C, Stengl M. 2009. Octopamine and tyramine modulate pheromone-sensitive olfactory sensilla of the hawkmoth *Manduca sexta* in a time-dependent manner. *J Comp Physiol A* **195**:529–545. doi:10.1007/s00359-009-0429-4

Fox RF, Lu Y. 1994. Emergent collective behavior in large numbers of globally coupled independently stochastic ion channels. *Phys Rev E* **49**:3421–3431. doi:10.1103/PhysRevE.49.3421

Géron A, Werner ,Johannes, Wattiez ,Ruddy, and Matallana-Surget S. 2024. Towards the discovery of novel molecular clocks in Prokaryotes. *Crit Rev Microbiol* **50**:491–503. doi:10.1080/1040841X.2023.2220789

Getahun MN, Olsson SB, Lavista-Llanos S, Hansson BS, Wicher D. 2013. Insect Odorant Response Sensitivity Is Tuned by Metabotropically Autoregulated Olfactory Receptors. *PLOS ONE* **8**:e58889. doi:10.1371/journal.pone.0058889

Getahun MN, Thoma M, Lavista-Llanos S, Keesey I, Fandino RA, Knaden M, Wicher D, Olsson SB, Hansson BS. 2016. Intracellular regulation of the insect chemoreceptor complex impacts odour localization in flying insects. *J Exp Biol* **219**:3428–3438. doi:10.1242/jeb.143396

Ghosh S, Suray C, Bozzolan F, Palazzo A, Monsempès C, Lecouvreur F, Chatterjee A. 2024. Pheromone-mediated command from the female to male clock induces and synchronizes circadian rhythms of the moth *Spodoptera littoralis*. *Curr Biol* **34**:1414-1425.e5. doi:10.1016/j.cub.2024.02.042

Goldstein SAN, Bockenhauer D, O'Kelly I, Zilberberg N. 2001. Potassium leak channels and the KCNK family of two-p-domain subunits. *Nat Rev Neurosci* **2**:175–184. doi:10.1038/35058574

Golowasch J, Bose A, Guan Y, Salloum D, Roeser A, Nadim F. 2017. A balance of outward and linear inward ionic currents is required for generation of slow-wave oscillations. *J Neurophysiol* **118**:1092–1104. doi:10.1152/jn.00240.2017

Guo H, Smith DP. 2022. Time-Dependent Odorant Sensitivity Modulation in Insects. *Insects* **13**:354. doi:10.3390/insects13040354

Guo H, Smith DP. 2017. Odorant Receptor Desensitization in Insects. *J Exp Neurosci* **11**:1179069517748600. doi:10.1177/1179069517748600

Hall JC, Rosbash M. 1993. Oscillating molecules and how they move circadian clocks across evolutionary boundaries. *Proc Natl Acad Sci U S A* **90**:5382–5383.

Hardin PE. 2011. Molecular Genetic Analysis of Circadian Timekeeping in *Drosophila* In: Brody S, editor. Advances in Genetics, The Genetics of Circadian Rhythms. Academic Press. pp. 141–173. doi:10.1016/B978-0-12-387690-4.00005-2

Hastings MH, Smyllie NJ, Patton AP. 2020. Molecular-genetic Manipulation of the Suprachiasmatic Nucleus Circadian Clock. *J Mol Biol* **432**:3639–3660. doi:10.1016/j.jmb.2020.01.019

Itagaki H, Conner WE. 1988. Calling Behavior of *Manduca sexta* (L.) (Lepidoptera: Sphingidae) with Notes on the Morphology of the Female Sex Pheromone Gland. *Ann Entomol Soc Am* **81**:798–807. doi:10.1093/aesa/81.5.798

750 Jain K, Lavista-Llanos S, Grabe V, Hansson BS, Wicher D. 2021. Calmodulin regulates the olfactory
751 performance in Drosophila melanogaster. *Sci Rep* **11**:3747. doi:10.1038/s41598-021-
752 83296-9
753 Jones PL, Pask GM, Rinker DC, Zwiebel LJ. 2011. Functional agonism of insect odorant receptor ion
754 channels. *Proc Natl Acad Sci* **108**:8821–8825. doi:10.1073/pnas.1102425108
755 Kaissling KE, Zack Strausfeld C, Rumbo ER. 1987. Adaptation processes in insect olfactory
756 receptors. Mechanisms and behavioral significance. *Ann N Y Acad Sci* **510**:104–112.
757 doi:10.1111/j.1749-6632.1987.tb43475.x
758 Krishnan B, Dryer SE, Hardin PE. 1999. Circadian rhythms in olfactory responses of *Drosophila*
759 *melanogaster*. *Nature* **400**:375–378. doi:10.1038/22566
760 Lamont EW, Amir S. 2010. Circadian and Ultradian Clocks/Rhythms In: Koob GF, Moal ML,
761 Thompson RF, editors. Encyclopedia of Behavioral Neuroscience. Oxford: Academic Press.
762 pp. 257–261. doi:10.1016/B978-0-08-045396-5.00223-2
763 Lee JK, Strausfeld NJ. 1990. Structure, distribution and number of surface sensilla and their
764 receptor cells on the olfactory appendage of the male mothManduca sexta. *J Neurocytol*
765 **19**:519–538. doi:10.1007/BF01257241
766 Livak KJ, Schmittgen TD. 2001. Analysis of relative gene expression data using real-time
767 quantitative PCR and the $2^{-\Delta\Delta C(T)}$ Method. *Methods San Diego Calif* **25**:402–408.
768 doi:10.1006/meth.2001.1262
769 Lüthi A, McCormick DA. 1998. H-Current: Properties of a Neuronal and Network Pacemaker.
770 *Neuron* **21**:9–12. doi:10.1016/S0896-6273(00)80509-7
771 Marion-Poll F, Tobin TR. 1992. Temporal coding of pheromone pulses and trains in *Manduca sexta*.
772 *J Comp Physiol A* **171**:505–512. doi:10.1007/BF00194583
773 Martín F, Charro M, Alcorta E. 2001. Mutations affecting the cAMP transduction pathway modify
774 olfaction in *Drosophila*. *J Comp Physiol A* **187**:359–370. doi:10.1007/s003590100208
775 Merlin C, François M-C, Queguiner I, Maïbèche-Coisné M, Jacquin-Joly E. 2006. Evidence for a
776 putative antennal clock in *Mamestra brassicae*: Molecular cloning and characterization of
777 two clock genes –*period* and *cryptochrome*– in antennae. *Insect Mol Biol* **15**:137–145.
778 doi:10.1111/j.1365-2583.2006.00617.x
779 Merlin C, Gegear RJ, Reppert SM. 2009. Antennal Circadian Clocks Coordinate Sun Compass
780 Orientation in Migratory Monarch Butterflies. *Science* **325**:1700–1704.
781 doi:10.1126/science.1176221
782 Merlin C, Lucas P, Rochat D, François M-C, Maïbèche-Coisne M, Jacquin-Joly E. 2007. An Antennal
783 Circadian Clock and Circadian Rhythms in Peripheral Pheromone Reception in the Moth
784 *Spodoptera littoralis*. *J Biol Rhythms* **22**:502–514. doi:10.1177/0748730407307737
785 Millar AJ. 2016. The Intracellular Dynamics of Circadian Clocks Reach for the Light of Ecology and
786 Evolution. *Annu Rev Plant Biol* **67**:595–618. doi:10.1146/annurev-arplant-043014-115619
787 Mönke G, Sorgenfrei FA, Schmal C, Granada AE. 2020. Optimal time frequency analysis for
788 biological data - pyBOAT. doi:10.1101/2020.04.29.067744
789 Mukunda L, Miazzi F, Kaltofen S, Hansson BS, Wicher D. 2014. Calmodulin modulates insect
790 odorant receptor function. *Cell Calcium* **55**:191–199. doi:10.1016/j.ceca.2014.02.013
791 Mukunda L, Miazzi F, Sargsyan V, Hansson BS, Wicher D. 2016. Calmodulin Affects Sensitization of
792 *Drosophila melanogaster* Odorant Receptors. *Front Cell Neurosci* **10**.
793 doi:10.3389/fncel.2016.00028
794 Nakagawa T, Vosshall LB. 2009. Controversy and consensus: noncanonical signaling mechanisms
795 in the insect olfactory system. *Curr Opin Neurobiol*, Signalling mechanisms **19**:284–292.
796 doi:10.1016/j.conb.2009.07.015

Nishiitsutsuji-Uwo J, Pittendrigh CS. 1968. Central nervous system control of circadian rhythmicity in the cockroach II. The pathway of light signals that entrain the rhythm. *Z Für Vgl Physiol* **58**:1–13. doi:10.1007/BF00302433

Nolte A, Funk NW, Mukunda L, Gawalek P, Werckenthin A, Hansson BS, Wicher D, Stengl M. 2013. In situ Tip-Recordings Found No Evidence for an Orco-Based Ionotropic Mechanism of Pheromone-Transduction in *Manduca sexta*. *PLOS ONE* **8**:e62648. doi:10.1371/journal.pone.0062648

Nolte A, Gawalek P, Koerte S, Wei H, Schumann R, Werckenthin A, Krieger J, Stengl M. 2016. No Evidence for Ionotropic Pheromone Transduction in the Hawkmoth *Manduca sexta*. *PLOS ONE* **11**:e0166060. doi:10.1371/journal.pone.0166060

Page TL, Koelling E. 2003. Circadian rhythm in olfactory response in the antennae controlled by the optic lobe in the cockroach. *J Insect Physiol* **49**:697–707. doi:10.1016/s0022-1910(03)00071-4

Patel AJ, Honoré E. 2001. Properties and modulation of mammalian 2P domain K+ channels. *Trends Neurosci* **24**:339–346. doi:10.1016/S0166-2236(00)01810-5

Pézier A, Acquistapace A, Renou M, Rospars J-P, Lucas P. 2007. Ca^{2+} Stabilizes the Membrane Potential of Moth Olfactory Receptor Neurons at Rest and Is Essential for Their Fast Repolarization. *Chem Senses* **32**:305–317. doi:10.1093/chemse/bjl059

Plautz JD, Kaneko M, Hall JC, Kay SA. 1997. Independent Photoreceptive Circadian Clocks Throughout *Drosophila*. *Science* **278**:1632–1635. doi:10.1126/science.278.5343.1632

Prosser RA, Gillette MU. 1991. Cyclic changes in cAMP concentration and phosphodiesterase activity in a mammalian circadian clock studied *in vitro*. *Brain Res* **568**:185–192. doi:10.1016/0006-8993(91)91396-I

Prosser RA, McArthur AJ, Gillette MU. 1989. cGMP induces phase shifts of a mammalian circadian pacemaker at night, in antiphase to cAMP effects. *Proc Natl Acad Sci U S A* **86**:6812–6815.

Pu S, Thomas PJ. 2020. Fast and Accurate Langevin Simulations of Stochastic Hodgkin-Huxley Dynamics. *Neural Comput* **32**:1775–1835. doi:10.1162/neco_a_01312

Ratliff J, Franci A, Marder E, O'Leary T. 2021. Neuronal oscillator robustness to multiple global perturbations. *Biophys J* **120**:1454–1468. doi:10.1016/j.bpj.2021.01.038

Redkozubov A. 2000. Guanosine 3',5'-Cyclic Monophosphate Reduces the Response of the Moth's Olfactory Receptor Neuron to Pheromone. *Chem Senses* **25**:381–385. doi:10.1093/chemse/25.4.381

Reinhard N, Fukuda A, Manoli G, Derksen E, Saito A, Möller G, Sekiguchi M, Rieger D, Helfrich-Förster C, Yoshii T, Zandawala M. 2024. Synaptic connectome of the *Drosophila* circadian clock. *Nat Commun* **15**:10392. doi:10.1038/s41467-024-54694-0

Riffell JA, Abrell L, Hildebrand JG. 2008. Physical processes and real-time chemical measurement of the insect olfactory environment. *J Chem Ecol* **34**:837–853. doi:10.1007/s10886-008-9490-7

Robinson RB, Siegelbaum SA. 2003. Hyperpolarization-activated cation currents: from molecules to physiological function. *Annu Rev Physiol* **65**:453–480. doi:10.1146/annurev.physiol.65.092101.142734

Sargsyan V, Getahun MN, Lavista Llanos S, Olsson SB, Hansson BS, Wicher D. 2011. Phosphorylation via PKC Regulates the Function of the *Drosophila* Odorant Co-Receptor. *Front Cell Neurosci* **5**. doi:10.3389/fncel.2011.00005

Sato K, Pellegrino M, Nakagawa Takao, Nakagawa Tatsuro, Vosshall LB, Touhara K. 2008. Insect olfactory receptors are heteromeric ligand-gated ion channels. *Nature* **452**:1002–1006. doi:10.1038/nature06850

Sauman I, Reppert SM. 1998. Brain Control of Embryonic Circadian Rhythms in the Silkmoth *Antheraea pernyi*. *Neuron* **20**:741–748. doi:10.1016/S0896-6273(00)81012-0

Schendzielorz J, Schendzielorz T, Arendt A, Stengl M. 2014. Bimodal Oscillations of Cyclic Nucleotide Concentrations in the Circadian System of the Madeira Cockroach *Rhyparobia maderae*. *J Biol Rhythms* **29**:318–331. doi:10.1177/0748730414546133

Schendzielorz T, Peters W, Boekhoff I, Stengl M. 2012. Time of Day Changes in Cyclic Nucleotides Are Modified via Octopamine and Pheromone in Antennae of the Madeira Cockroach. *J Biol Rhythms* **27**:388–397. doi:10.1177/0748730412456265

Schendzielorz T, Schirmer K, Stolte P, Stengl M. 2015. Octopamine Regulates Antennal Sensory Neurons via Daytime-Dependent Changes in cAMP and IP_3 Levels in the Hawkmoth *Manduca sexta*. *PLOS ONE* **10**:e0121230. doi:10.1371/journal.pone.0121230

Schmidt DR, Galán RF, Thomas PJ. 2018. Stochastic shielding and edge importance for Markov chains with timescale separation. *PLOS Comput Biol* **14**:e1006206. doi:10.1371/journal.pcbi.1006206

Schmidt DR, Thomas PJ. 2014. Measuring Edge Importance: A Quantitative Analysis of the Stochastic Shielding Approximation for Random Processes on Graphs. *J Math Neurosci* **4**:6. doi:10.1186/2190-8567-4-6

Schneider AC, Schröder K, Chang Y, Nolte A, Gawalek P, Stengl M. 2025. Hawkmoth Pheromone Transduction Involves G-Protein–Dependent Phospholipase Cβ Signaling. *eNeuro* **12**:ENEURO.0376-24.2024. doi:10.1523/ENEURO.0376-24.2024

Schuckel J, Siwicki KK, Stengl M. 2007. Putative circadian pacemaker cells in the antenna of the hawkmoth *Manduca sexta*. *Cell Tissue Res* **330**:271–278. doi:10.1007/s00441-007-0471-x

Sharma A, Rahman G, Gorelik J, Bhargava A. 2023. Voltage-Gated T-Type Calcium Channel Modulation by Kinases and Phosphatases: The Old Ones, the New Ones, and the Missing Ones. *Cells* **12**:461. doi:10.3390/cells12030461

Silvegren G, Löfstedt C, Qi Rosén W. 2005. Circadian mating activity and effect of pheromone pre-exposure on pheromone response rhythms in the moth *Spodoptera littoralis*. *J Insect Physiol* **51**:277–286. doi:10.1016/j.jinsphys.2004.11.013

Stengl M. 2010. Pheromone Transduction in Moths. *Front Cell Neurosci* **4**:133. doi:10.3389/fncel.2010.00133

Stengl M. 1994. Inositol-trisphosphate-dependent calcium currents precede cation currents in insect olfactory receptor neurons *in vitro*. *J Comp Physiol A* **174**:187–194. doi:10.1007/BF00193785

Stengl M. 1993. Intracellular-Messenger-Mediated Cation Channels in Cultured Olfactory Receptor Neurons. *J Exp Biol* **178**:125–147. doi:10.1242/jeb.178.1.125

Stengl M, Funk NW. 2013. The role of the coreceptor Orco in insect olfactory transduction. *J Comp Physiol A* **199**:897–909. doi:10.1007/s00359-013-0837-3

Stengl M, Schneider AC. 2024. Contribution of membrane-associated oscillators to biological timing at different timescales. *Front Physiol* **14**:1243455. doi:10.3389/fphys.2023.1243455

Stengl M, Schröder K. 2021. 14 - Multiscale timing of pheromone transduction in hawkmoth olfactory receptor neurons. In: Blomquist GJ, Vogt RG, editors. Insect Pheromone Biochemistry and Molecular Biology (Second Edition). London: Academic Press. pp. 435–468. doi:10.1016/B978-0-12-819628-1.00014-6

Stengl M, Zintl R, De Vente J, Nighorn A. 2001. Localization of cGMP immunoreactivity and of soluble guanylyl cyclase in antennal sensilla of the hawkmoth Manduca sexta. *Cell Tissue Res* **304**:409–421. doi:10.1007/s004410000336

890 Szyszka P, Gerkin RC, Galizia CG, Smith BH. 2014. High-speed odor transduction and pulse
891 tracking by insect olfactory receptor neurons. *Proc Natl Acad Sci* **111**:16925–16930.
892 doi:10.1073/pnas.1412051111
893 Talley EM, Solórzano G, Lei Q, Kim D, Bayliss DA. 2001. CNS Distribution of Members of the Two-
894 Pore-Domain (KCNK) Potassium Channel Family. *J Neurosci* **21**:7491–7505.
895 doi:10.1523/JNEUROSCI.21-19-07491.2001
896 Tanoue S, Krishnan P, Krishnan B, Dryer SE, Hardin PE. 2004. Circadian Clocks in Antennal
897 Neurons Are Necessary and Sufficient for Olfaction Rhythms in *Drosophila*. *Curr Biol*
898 **14**:638–649. doi:10.1016/j.cub.2004.04.009
899 Thaiss CA, Zeevi D, Levy M, Zilberman-Schapira G, Suez J, Tengeler AC, Abramson L, Katz MN,
900 Korem T, Zmora N, Kuperman Y, Biton I, Gilad S, Harmelin A, Shapiro H, Halpern Z, Segal E,
901 Elinav E. 2014. Transkingdom Control of Microbiota Diurnal Oscillations Promotes
902 Metabolic Homeostasis. *Cell* **159**:514–529. doi:10.1016/j.cell.2014.09.048
903 Tripathy S, Staudacher EM, Peters O, Kalwar F, Hatfield M, Daly K. 2010. Odors pulsed at wing beat
904 frequencies are tracked by primary olfactory networks and enhance odor detection. *Front*
905 *Cell Neurosci* **4**. doi:10.3389/neuro.03.001.2010
906 Viertel R, Borisyuk A. 2019. A Computational model of the mammalian external tufted cell. *J Theor*
907 *Biol* **462**:109–121. doi:10.1016/j.jtbi.2018.10.003
908 Wicher D, Miazzi F. 2021. Functional properties of insect olfactory receptors: ionotropic receptors
909 and odorant receptors. *Cell Tissue Res* **383**:7–19. doi:10.1007/s00441-020-03363-x
910 Wicher D, Schäfer R, Bauernfeind R, Stensmyr MC, Heller R, Heinemann SH, Hansson BS. 2008.
911 *Drosophila* odorant receptors are both ligand-gated and cyclic-nucleotide-activated cation
912 channels. *Nature* **452**:1007–1011. doi:10.1038/nature06861
913 Zhou X, Yuan C, Guo A. 2005. *Drosophila* Olfactory Response Rhythms Require Clock Genes but
914 Not Pigment Dispersing Factor or Lateral Neurons. *J Biol Rhythms* **20**:237–244.
915 doi:10.1177/0748730405274451
916 Ziegelberger G, Berg M van den, Kaissling KE, Klumpp S, Schultz JE. 1990. Cyclic GMP levels and
917 guanylate cyclase activity in pheromone-sensitive antennae of the silkmoths *Antheraea*
918 *polyphemus* and *Bombyx mori*. *J Neurosci* **10**:1217–1225. doi:10.1523/JNEUROSCI.10-04-
919 01217.1990
920 Zufall F, Stengl M, Franke C, Hildebrand JG, Hatt H. 1991. Ionic currents of cultured olfactory
921 receptor neurons from antennae of male Manduca sexta. *J Neurosci* **11**:956–965.
922 doi:10.1523/JNEUROSCI.11-04-00956.1991
923

8 Figures and Figure legends

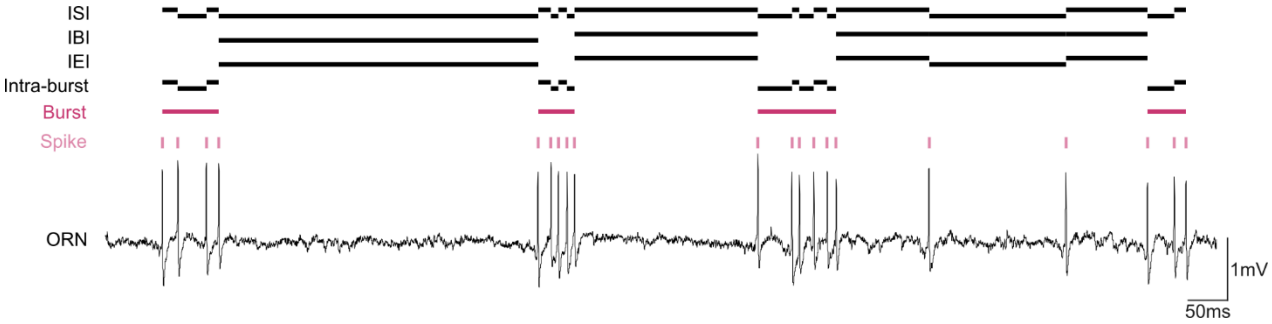

Figure 1: Attributes of pheromone-sensitive ORN spiking patterns.

Spikes were identified by their prominence in the raw ORN recording. The inter-spike interval (ISI) was defined as the time from one spike to the next. A train with ≥2 spikes with ISI ≤ 50 ms was considered a burst. The intra-burst interval was the ISIs within a burst, the inter-burst interval (IBI) the ISIs between two bursts, omitting any individual spikes in between. The inter-event interval (IEI) included the ISIs between bursts and individual spikes.

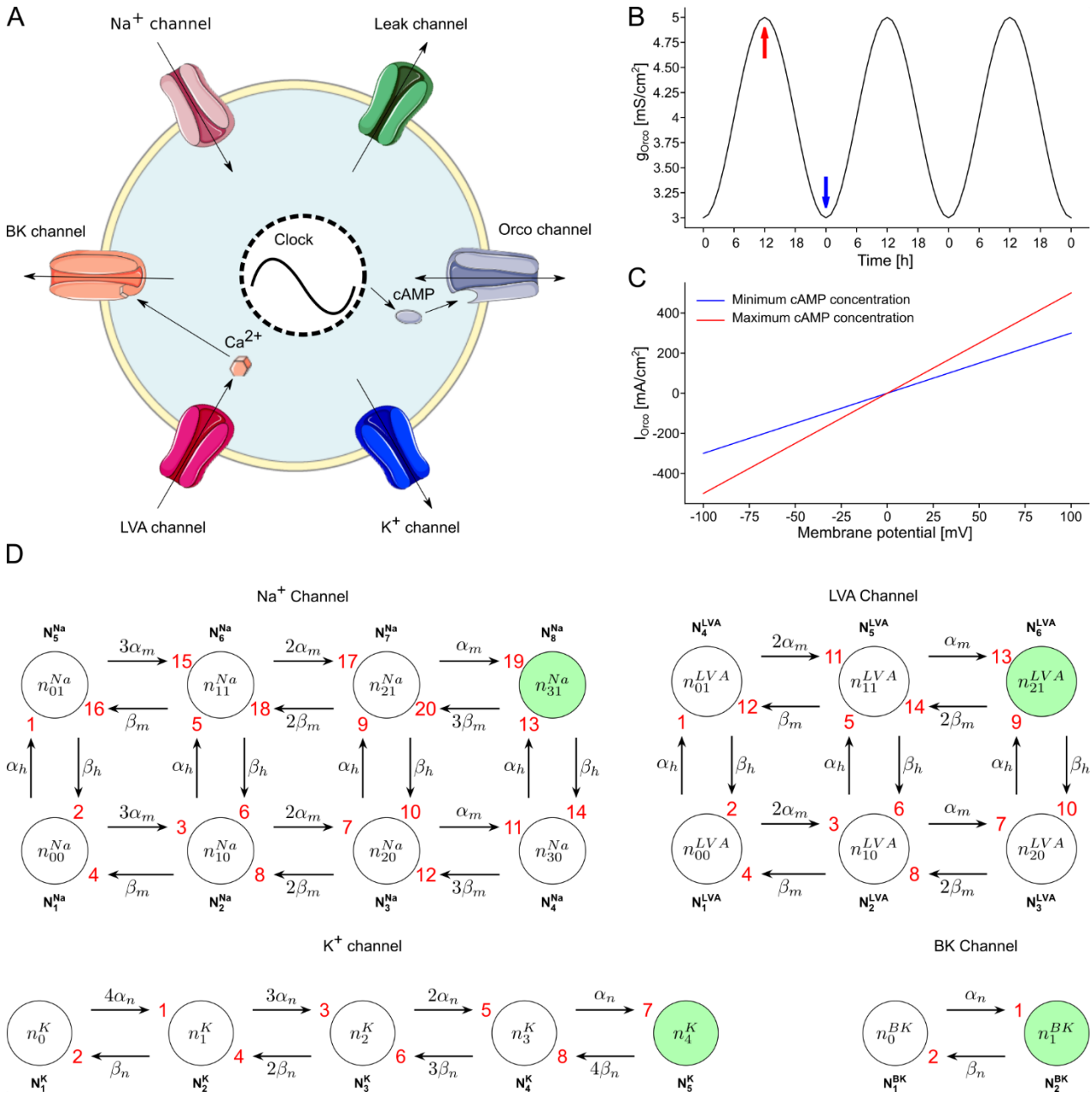

933

934 **Figure 2: The conductance-based model of a simplified hawkmoth ORN.**

935 **(A)** Schematic of the model containing a voltage gated sodium channel (Na^+), a voltage gated
936 potassium channel (K^+), a low voltage activated calcium channel (LVA), a calcium and voltage
937 activated potassium channel (BK), a leak channel, and a cAMP-gated leaky non-specific cation
938 channel (Orco). The Orco channel is represented as a linear conductance whose value oscillates
939 with a sinusoidal shape as a function of the ZT. The circadian rhythm in the Orco conductance is
940 hypothesized to result from a cAMP-dependent increase in channel open-time probability (as
941 found in *Drosophila* Orco: (Getahun et al., 2013)) via a circadian oscillation of antennal cAMP
942 concentrations (Schendzielorz et al., 2015). This oscillation is driven by the circadian clock and
943 serves as an input; the internal mechanism of the clock is not modeled explicitly. Arrows indicate
944 the flow of ions through the channels. **(B)** Parametrized circadian oscillation in Orco conductivity,

945 introduced as an external input to our model, representing the gating of Orco by cAMP whose
946 concentration oscillates on a circadian timescale. The times of minimum and maximum cAMP
947 concentration are indicated by colored arrows. **(C)** Parametrized IV curve of the Orco channel
948 showing a linear behavior with the slope depending on the cAMP concentration. Line colors
949 correspond to the arrows in panel B. **(D)** Markov-chain representing all possible states and
950 transitions for each type of ion channel included in the model. The per capita transition rates (α and
951 β) depend on membrane potential and in the case of the BK channel also on the intracellular Ca^{2+}-
952 concentration. The "N" state vectors contain the population of channels in each state "n".
953 Subscripts of "n" indicate how many activation and inactivation gates are in the open state.
954 Directed edges are numbered in red. The only conducting state of each ion channel, representing
955 the condition where all its gates are open, is shown in green. Panel **A** was drawn using pictures
956 from Servier Medical Art. Servier Medical Art by Servier is licensed under a Creative Commons
957 Attribution 3.0 Unported License.

958

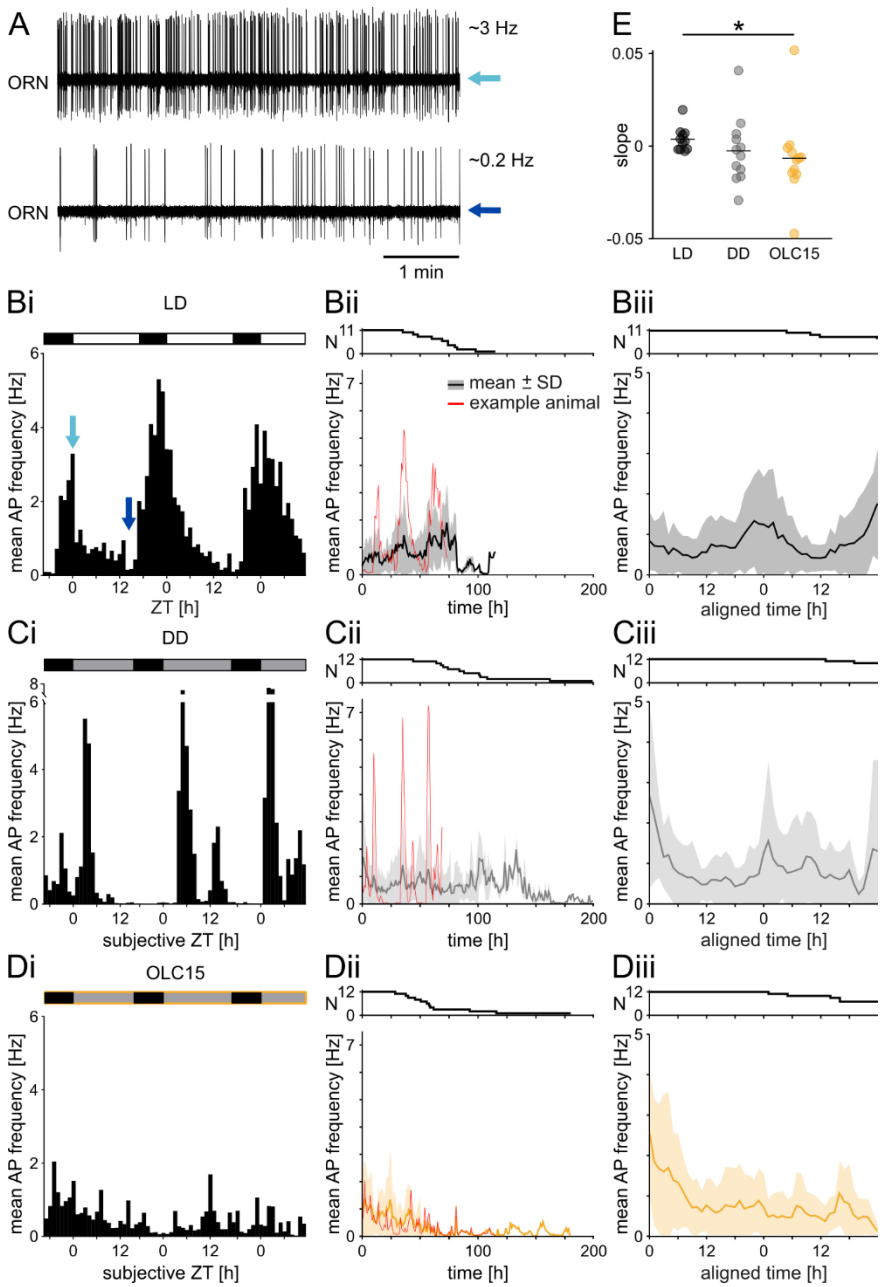

Figure 3: Spontaneous activity of pheromone-sensitive olfactory receptor neurons (ORNs) of male *M. sexta* shows Orco-dependent circadian modulation.

(A) Example tip recordings of the spontaneous activity of one long trichoid sensillum during a period of high (top, average frequency ~ 3 Hz) and low (bottom, average frequency ~ 0.2 Hz) activity. **(Bi)** Spontaneous spike frequency of one long-term ORN recording during 17:7 light-dark cycles (same experiment as in **A,** colored arrows indicate respective zeitgeber times (ZT)), indicated by the black-white bar at the top, increased during each activity phase and was low during the resting phases. Spike frequencies were averaged for each 1 h bin. **(Bii)** Mean spontaneous ORN spike frequency across all LD animals in 1 h bins. Data from the individual in Bi is highlighted in red. Recordings had different lengths, therefore the number of recordings used for the element-wise mean for each 1 h bin decreased with the time since the start of the recording, indicated in the top

panel. **(Biii)** Mean spontaneous ORN spike frequency across all LD animals in 1 h bins during the first 48 hours revealed circadian activity. **(Ci)** The spontaneous spike frequency of one long-term ORN recording in constant darkness (DD, the expected times of lights on are represented by grey bars above) exhibited a circadian pattern. The peak activity shifted in DD due to the animal's endogenous, free-running circadian period $\tau = 21.27$ h. **(Cii)** Mean spontaneous ORN spike frequency across all DD animals in 1 h bins. Data from the individual in Ci is highlighted in red. **(Ciii)** Mean spontaneous ORN spike frequency across all DD animals in 1 h bins during the first 48 hours after aligning the time to the first maximum in spontaneous activity (see Methods) revealed circadian activity. **(Di)** The spontaneous spike frequency of one long-term ORN recording in constant darkness with infusion of the Orco antagonist OLC15 (orange frame) dissipated the circadian rhythm of spontaneous activity. **(Dii)** Mean spontaneous ORN spike frequency across all OLC15 animals in 1 h bins. Data from the individual in Di is highlighted in red. In contrast to LD and DD conditions, the spike frequency decreases over time with prolonged exposure to OLC15. **(Diii)** Mean spontaneous ORN spike frequency across all OLC15 animals in 1 h bins (mean ± SD) during the first 48 hours after aligning the time to the first maximum in spontaneous activity (see Methods). In contrast to LD and DD conditions, the circadian change in spontaneous spiking frequency disappeared. **(E)** The slopes of the linear fits to the binned spiking activity of each individual animal in the three different conditions (see Methods). Each dot indicates the slope for one experiment. The line indicates the mean. The slope for OLC15 is significantly different from control LD.

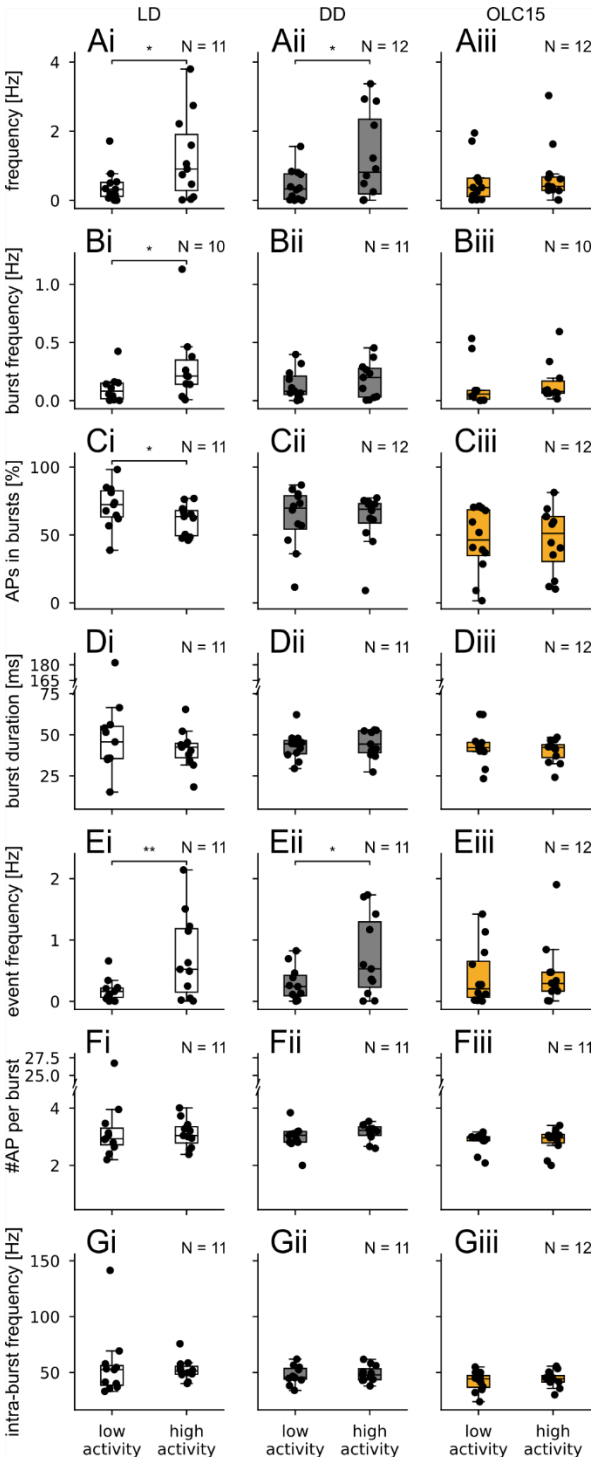

992

993 **Figure 4: Blocking Orco removed circadian modulation of spontaneous ORN spiking patterns.**
994 Some attributes of the spontaneous ORN activity were significantly different (Wilcoxon signed-rank
995 test, α = 0.05) between the time windows of low vs. high activity, mostly in LD (white boxes) and DD
996 (gray boxes) conditions, but never when Orco was blocked with OLC15 (orange boxes). In both LD
997 and DD, the mean spiking frequency was increased during high activity (**Ai, Aii**)**.** Only in LD but not
998 in DD, the mean inter-burst intervals (IBI; **Bi, Bii**), the relative number of spikes belonging to a burst

(**Ci, Cii**) and the mean inter-event interval (IEI; **Di, Dii**) decreased significantly during the high activity period. Both in LD and DD the mean burst duration (**Ei,Eii**), mean number of spikes per bust (**Fi,Fii**), and mean intra-burst intervals (**Gi, Gii**) did not differ between low vs. high spiking activity. Also, with Orco blocking, the attributes for low vs. high activity did not differ for any of the attributes tested (**Aiii-Giii**). In DD and OLC15conditions, activity phases were aligned as described in the Methods; thus, low activity in DD was at subjective ZT 19 and in OLC15 at subjective ZT 13, high activity was in both cases at subjective ZT 24. ZTs for low and high activity in LD were 10 and 0, respectively.

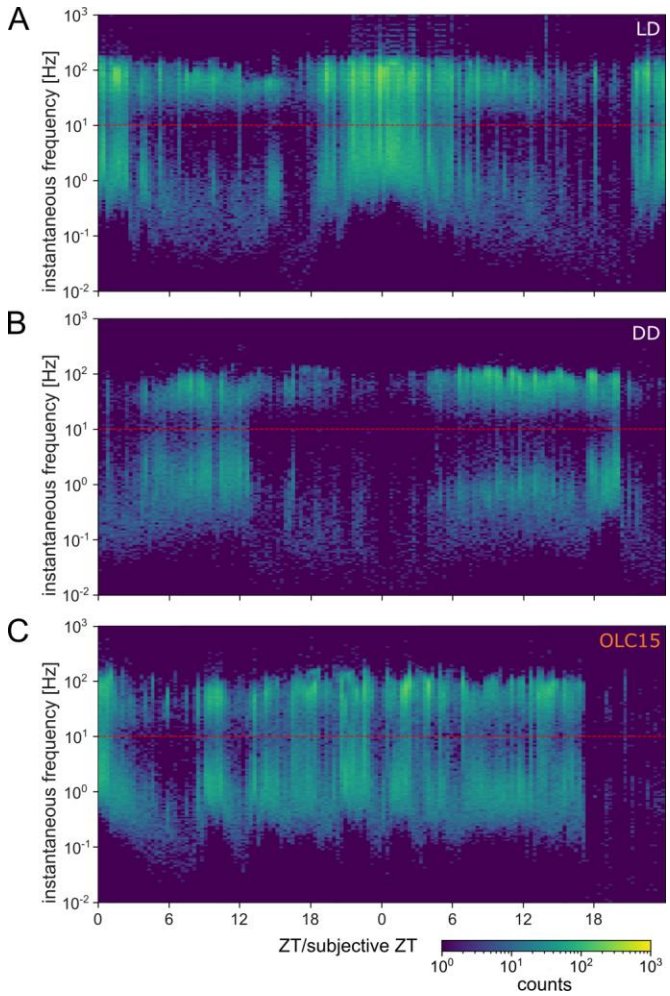

Figure 5: Blocking Orco removed circadian regulation of ultradian rhythms in the spontaneous ORN spiking pattern.

Heat map of the instantaneous frequencies (1/ISI) over two consecutive days of long-term tip-recordings of one pheromone-sensitive long trichoid sensillum under different conditions (LD **(A)**, DD **(B)**, OLC15 **(C)**) in each panel. Pixel color indicates the counts of instantaneous frequencies in that respective bin. The points fall mostly in a band of high frequencies (>10 – ~100 Hz) and low frequencies (0.01 – ~10 Hz), with the high-frequency band representing the instantaneous frequencies of spikes within a burst and the low-frequency band the instantaneous frequency between bursts. **(A, B)** The high frequency band indicates daily and circadian modulation of frequency prevalence. In addition, the low frequency band (<0.01 Hz to ~ 10 Hz) also displayed circadian modulation of the frequency composition. **(C)** Infusion of OLC15 deleted the circadian modulation in both frequency bands and enhanced the ultradian rhythm of frequency prevalence.

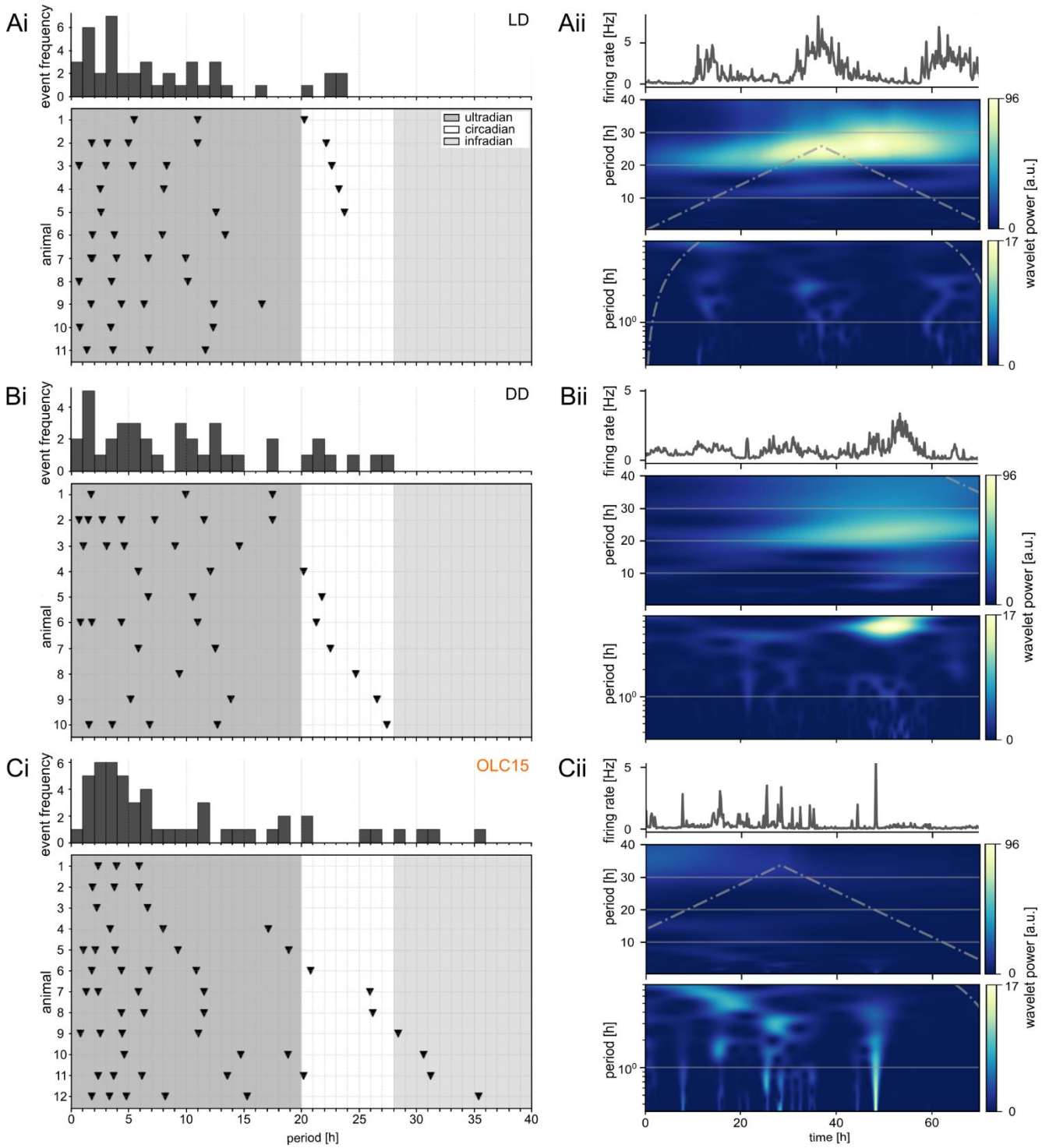

Figure 6: Blocking Orco affected ultradian and infradian frequencies in the spontaneous ORN firing patterns.

The Fourier analysis of spontaneous spiking activity revealed rhythms with ultradian (<20 h; dark grey), circadian (20-28 h; white), and infradian periods (>28 h; light grey) in LD (**Ai**), DD (**Bi**), and OLC15 (**Ci**). Each line represents one animal where each triangular marker is at the local maximum in the frequency spectra obtained for that animal. The histograms above illustrate how often

specific periods of spiking activity rhythms occurred averaged over all animals. Circadian rhythms were detected in LD (N = 5 of 11), DD (N = 7 of 10), and OLC15 (N = 4 of 12). Wavelet analysis of LD (**Aii**), DD (**Bii**), and OLC15 (**Cii**) confirmed the occurrence of multiscale periods. Example plots for one animal each, the same animals as in Figure 5. For each panel, the top plot depicts the mean firing frequency, the middle plot the wavelet power in the same period range as panels **i**, and the bottom plot the wavelet power for infradian periods up to 7 h on a log scale to highlight infradian time scales.

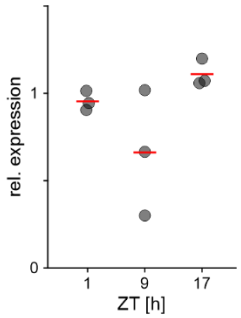

1037

1038 **Figure 7: Orco is not under control of the TTFL-based molecular circadian clock.**
1039 Relative expression levels of *Orco* mRNA from male hawkmoth antennae raised under LD
1040 conditions did not differ significantly (ANOVA on ranks, $H(2) = 5.60$, $p = 0.061$) between ZT 1 (end of
1041 activity phase), ZT 9 (resting phase), and ZT 17 (beginning of the activity phase). *timeless* mRNA
1042 levels from male hawkmoth antenna served as control and were published in Schneider et al.
1043 (2025).

1044

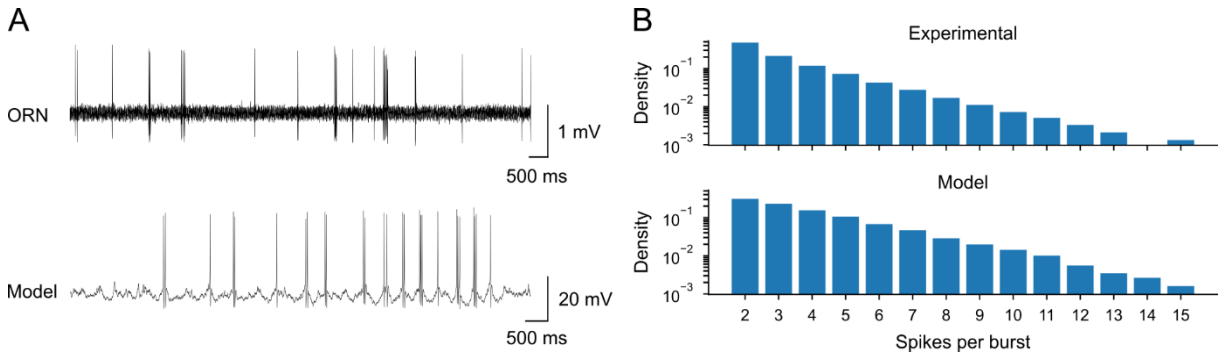

Figure 8: The model adequately reproduces the firing pattern of the biological ORN. **(A)** The model activity (bottom trace) displays both isolated spikes and bursts of variable length as in the original recording (top trace). The model represents an intracellular recording whereas the biological recordings were done with extracellular electrodes. **(B)** Semi-logarithmic plot of burst length distribution of an experimental LD recording (top) and simulated model (bottom) of spontaneous action potential activity of pheromone-sensitive neurons. Both the model and the recordings display exponential decrease of the count's density as a function of the burst length, shown as a linear decrease in the logarithmic scale.

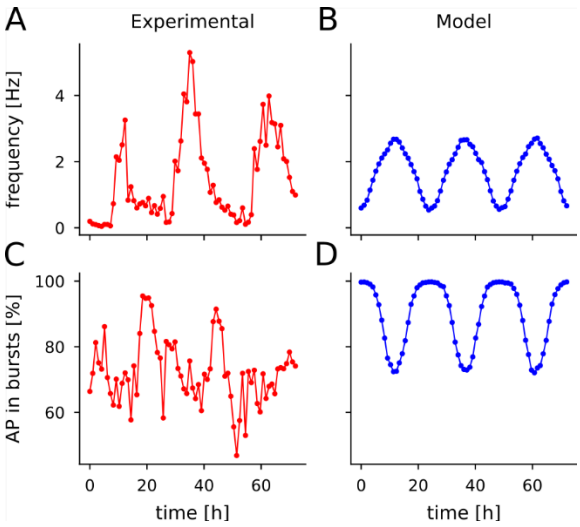

Figure 9: Comparison of the circadian modulation of model and ORN spiking attributes. Mean spike frequency and percentage of spikes that belong to bursts show anti-phasic circadian oscillations both in the simulated model (left) and in the biological recording (right).

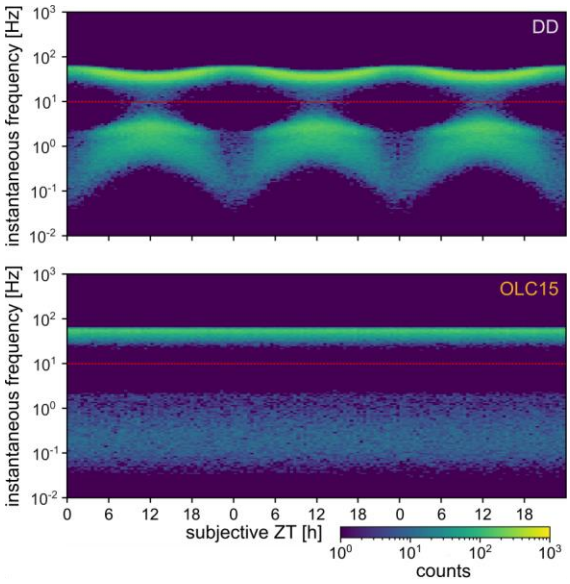

Figure 10: The model captures the Orco-dependent circadian modulation of ultradian spiking rhythms.

Heat map of the simulated model, pixel color indicates the density of instantaneous frequencies in that respective bin. The points can be roughly divided in a band of high frequencies (top, ~50 – 80 Hz) and low frequencies (bottom, ~0.1 – 5 Hz), with the high-frequency band representing the instantaneous frequencies of spikes within a burst and the low-frequency band the instantaneous frequency between bursts. **(A)** Simulated spikes with circadian regulation by the Orco channel; the inter-burst frequencies varied widely with circadian rhythmicity while the frequencies within burst remained approximately constant. The simulated results also reproduced the "merging" effect between the two bands when the bottom one approaches the top one. **(B)** Simulated spikes without circadian regulation of Orco had no circadian oscillations.

9 Supplementary Material

9.1 Mathematical Model

The mathematical model is a 22-dimensional system of stochastic differential equations designed to describe the behavior of ion channels and their effects on the membrane potential. I_{LVA} represents a low-voltage-activated calcium current, while I_{Na} and I_K are the transient sodium and potassium currents responsible for action potential generation. I_{BK} is a large-conductance potassium channel that is activated by both a depolarized membrane potential and an increased intracellular calcium concentration, and I_L is the leak current. Additionally, the Orco channel is a leaky, non-specific ion channel gated by cAMP, with the cAMP concentration oscillating in a circadian rhythm. To model the Orco conductance, we used a sinusoidal function of Zeitgeber time (ZT), independent of the membrane potential, as shown in Figure 2B, C. Each of these ion channels has been reported in vitro in previous studies (Dolzer et al., 2021).

The deterministic part of the 22D model is given by the mean field of the channel-based Langevin model. This approach was introduced by Fox and Lu's (1994) for a 14D HH model. In their framework, one dimension tracks the membrane potential, while the other 13 dimensions correspond to the fraction of channels in each of the five states in the potassium (K^+) Markov chain and the eight states in the sodium (Na^+) Markov chain. Pu and Thomas (2020) demonstrated that the deterministic 14D model and the original 4D HH model are dynamically equivalent, meaning that each solution of the 4D model corresponds to a solution of the 14D model.

Expanding upon Pu and Tomas' methodology to represent out system, we added one dimension to track the calcium concentration, six dimensions for each possible state of the LVA channel, and two dimensions for each possible state of the BK channel. The state vectors for each ion channel are therefore defined as follows: a five-component vector NK for the K^+ gates, an eight-component vector NNa for the Na^+ gates, a six-component vector NLVA for the LVA gates, and a two-component vector NBK for the BK gates. The state vectors are represented as:

$$N^K = [n_{K0}, n_{K1}, n_{K2}, n_{K3}, n_{K4}]^T \in [0,1]^5 \quad (1)$$

$$N^{Na} = [n_{Na00}, n_{Na10}, n_{Na20}, n_{Na30}, n_{Na01}, n_{Na11}, n_{Na21}, n_{Na31}]^T \in [0,1]^8 \quad (2)$$

$$N^{LVA} = [n_{LVA00}, n_{LVA10}, n_{LVA20}, n_{LVA01}, n_{LVA11}, n_{LVA21}]^T \in [0,1]^6 \quad (3)$$

$$N^{BK} = [n_{BK0}, n_{BK1}]^T \in [0,1]^2 \quad (4)$$

The K^+ channel consists of four independent n (activation) gates, forming a five-vertex channel-state diagram with eight directed edges. The channel conducts a current only when it is in the rightmost state (Figure 2D). Similarly, the Na^+ channel is composed of three identical n gates and one h (inactivation) gate, forming an 8-vertex diagram with 20 directed edges, one of which is conducting. The LVA channel includes two identical n gates and one h gate, resulting in a 6-vertex diagram with 14 directed edges, one of which is conducting. The BK channel consists of a single n gate, forming a 2-vertex diagram with two directed edges, one of which is conducting. The Markov chain for every channel is shown in Figure 2B.

For a sufficiently large number of channels, Schmidt and Thomas (2014) and Schmidt et al. (2018) demonstrated that, under voltage clamp, the equations governing the system can be approximated by a multidimensional Ornstein-Uhlenbeck (OU) process, or Langevin equation, as follows:

$$dN^{ion} = \sum_{k=1}^{k_{max}} \zeta^{ion} \left\{ \alpha_k^{ion}(V) N_{i(k)}^{ion} dt + \sqrt{\epsilon^{ion} \alpha_k^{ion} \, N_{i(k)}^{ion} \, dW_k^{ion}} \right\} \tag{5}$$

Here ζ^{ion} is the stoichiometry vector for the kth directed edge. If we write i(k) for the source node and j(k) for the destination node of edge k, then $\zeta^{ion} = e_{j(k)}^{ion} - e_{i(k)}^{ion}$. The voltage-dependent per capita transition rate along the kth edge is $\alpha_k^{ion}(V)$ and $N_{i(k)}^{ion}$ is the fractional occupancy of the source node for the kth transition. The finite-time increment in the Poisson process is approximated by a gaussian process, namely, the increment dW_k^{ion} in a Wiener (Brownian motion) process associated with each directed edge. These independent noise terms are scaled by $\epsilon^{ion} = \frac{1}{N_{Tot}^{ion}}$, where $\frac{1}{N_{Tot}^{ion}}$ represents the total number of that specific ion channel.

The membrane potential is governed by the current balance equation:

$$C \frac{dV}{dt} = \sum_{\chi} I_{\chi} \tag{6}$$

where the set χ contains the six ionic currents included in the model:

$$\chi \in \{LVA, Na, K, BK, L, ORCO\} \tag{7}$$

Each of the six ionic currents included in the model are described as:

$$I_{Na} = -g_{Na} N_8^{Na} (V - V_{Na}) \quad (8)$$

$$I_K = -g_K N_5^K (V - V_K) \quad (9)$$

$$I_{LVA} = -g_{LVA} N_6^{LVA} (V - V_{LVA}) \quad (10)$$

$$I_{BK} = -g_{BK} N_2^{BK} (V - V_{BK}) \quad (11)$$

$$I_{Orco} = -g_{Orco} \left(0.8 + 0.2\, sin\left(\frac{2\pi t}{24h}\right)\right) (V - V_{Orco}) \quad (12)$$

$$I_L = -g_L (V_L - V) \quad (13)$$

Here, g_χ is the maximal conductance, V is the membrane potential, and V_χ is the reversal potential for each ion current. The parameter values for each current can be found in Table 1.

Each transition rate $\alpha_k^{ion}(V)$ is calculated in the following way:

$$\alpha_k^{ion}(V) = \frac{p_{j(k)\infty}^{ion}(V)}{\tau_p(V)} \quad (14)$$

where $p_{j(k)\infty}^{ion}(V)$ is the steady state value of the specific gate that switches states in the destination state and $\tau_p(V)$ is the time constant of said gate. The steady state activation values and time constants for the LVA, Na, K, and BK channels were based on Viertel and Borisyuk (2019). The steady state functions for the activation gates are denoted with m_∞^{ion}, and those for the inactivation gates with h_∞^{ion}.

Each gate's steady state activation function, except for the BK channel, takes the form:

$$p_{j\infty}^{ion}(V) = \frac{1.0}{1.0 + exp\left(\frac{(V - \theta_p)}{\beta_p}\right)} \quad (15)$$

The I_{BK} current is dependent on the intracellular calcium concentration and membrane potential as represented by the following equations:

$$m_{\infty}^{BK}(V) = \frac{1.0}{1.0 + exp\left(\frac{\left(V - V_{\frac{1}{2}}\right)}{(-15.6)}\right)} \tag{16}$$

$$V_{\frac{1}{2}} = -20 + 59.2e^{-90[Ca]} + 96.7e^{-470[Ca]} \tag{17}$$

$$\tau_{\alpha} = -(q - 1.0)\frac{(f - 0.2)}{0.8} + 170 \tag{18}$$

$$q = 2.9 + 6.3e^{-360[Ca]} \tag{19}$$

$$s = -25.3 + 107.5e^{-120[Ca]} \tag{20}$$

$$f = \frac{1.0}{10.0\left(e^{\frac{-(V+100.0-s)}{63.6}} + e^{\frac{(-150.0+(V+100.0-s))}{63.6}}\right)} \tag{21}$$

The intracellular concentration of calcium ions is described by the following equation:

$$\frac{d[Ca]}{dt} = -\gamma\frac{I_{LVA}}{zFd} + \frac{[Ca_0] - [Ca]}{\tau_{Ca}} \tag{22}$$

where Ca_0 is the steady state calcium concentration, γ describes calcium buffering, z is the ionic valence of calcium, F is Faraday's constant and d is the depth in microns at which calcium ions concentrate near the membrane.

The parameters of each steady state activation function as well as the time constant for each gating value can be found in Table 2.

Table 1: Parameter values for model currents.

Current	g_X (mS/cm^2)	V_X (mV)
I_L	4.3	-62.5
I_{LVA}	10.0	120
I_{NA}	29.17	45.0
I_K	12.96	-105.0
I_{BK}	9.0	-105.0
I_{ORCO}	5.0	0.0

Table 2: Gating variable parameter values.

Variable	θ	β	τ(ms)

m^{LVA}	-30	-4.8916	$\frac{40.0}{cosh\left(\frac{(V+37.1)}{9.7832}\right)}$
h^{LVA}	-59.2	11.2326	$\frac{350.0}{cosh\left(\frac{(V+59.2)}{22.4652}\right)}$
m^{Na}	-25.0	-6.5	0.2
h^{Na}	-26.0	9.0	$\frac{10.0}{cosh\left(\frac{(V+26.0)}{18.0}\right)}$
m^{K}	-26.0	-9.0	$\frac{10.0}{cosh\left(\frac{(V+26.0)}{18.0}\right)}$